

Thermal infrared dust optical depth and coarse-mode effective diameter over oceans retrieved from collocated MODIS and CALIOP observations

5 Jianyu Zheng^{1,2}, Zhibo Zhang^{1,2,*}, Hongbin Yu³, Anne Garnier^{4,5}, Qianqian Song^{1,2,a}, Chenxi Wang^{2,3}, Claudia Di Biagio⁶, Jasper F. Kok⁷, Yevgeny Derimian⁸, Claire Ryder⁹

¹Department of Physics, University of Maryland Baltimore County, Baltimore, MD 21250, USA

²Goddard Earth Sciences Technology and Research II, University of Maryland Baltimore County, Baltimore, MD 21250, USA

³NASA Goddard Space Flight Center, Greenbelt, MD 20771, USA

⁴Science Systems and Applications, Inc., Hampton, VA, USA

⁵NASA Langley Research Center, Hampton, VA, USA

⁶Université Paris Cité and Univ Paris Est Creteil, CNRS, LISA, F-75013 Paris, France

⁷Department of Atmospheric and Oceanic Sciences, University of California, Los Angeles, CA 90095, USA

⁸French National Centre for Scientific Research | CNRS · Laboratoire d'optique atmosphérique (LOA)

⁹Department of Meteorology, University of Reading, Reading, UK.

^a Now at: [Atmospheric and Oceanic Sciences Program, Princeton University, Princeton, NJ 08544, USA](#)

20 Correspondence to: Zhibo Zhang (zzbatmos@umbc.edu)

Formatted: English (United Kingdom)

Abstract.

In this study, we developed a novel algorithm based on the collocated Moderate Resolution Imaging Spectroradiometer (MODIS) thermal infrared (TIR) observations and dust vertical profiles from the Cloud-Aerosol Lidar with Orthogonal Polarization (CALIOP) to simultaneously retrieve dust aerosol optical depth at 10 μm (DAOD_{10 μm}) and the coarse-mode dust effective diameter (D_{eff}) over global oceans. The accuracy of the D_{eff} retrieval is assessed by comparing the [dust lognormal volume particle size distribution \(PSD\)](#) ~~PSD~~ corresponding to retrieved D_{eff} with the in-situ measured dust ~~partiele size distributions (PSDs)~~ ~~PSDs~~ from the AER-D, SAMUM-2 and SALTRACE field campaigns through case studies. The new DAOD_{10 μm} retrievals were evaluated first through comparisons with the collocated DAOD_{10.6 μm} retrieved from the combined Imaging Infrared Radiometer (IIR) and CALIOP observations from our previous study (Zheng et al. 2022). The pixel-to-pixel comparison of the two [DAOD](#) retrievals indicates a good agreement ($R \sim 0.7$) and a significant reduction of ($\sim 50\%$) retrieval uncertainties largely thanks to the better constraint on dust size. In a climatological comparison, the seasonal and regional ($5^\circ \times 2^\circ$) mean DAOD_{10 μm} retrievals based on our combined MODIS and CALIOP method are in good agreement with the two independent Infrared Atmospheric Sounding Interferometer (IASI) products over three dust transport regions (i.e., North Atlantic (NA; $R = 0.9$), Indian Ocean (IO; $R = 0.8$) and North Pacific (NP; $R = 0.7$)).

Using the new retrievals from 2013 to 2017, we performed a climatological analysis of coarse mode dust D_{eff} over global oceans. We found that dust D_{eff} over IO and NP are up to 20% smaller than that over NA. Over NA in summer, we found a $\sim 50\%$ reduction of the number of retrievals with $D_{\text{eff}} > 5 \mu\text{m}$ from 15°W to 35°W and a stable trend of D_{eff} average at 4.4 μm from 35°W throughout the Caribbean Sea (90°W). Over NP in spring, only $\sim 5\%$ of retrieved pixels

40 with $D_{\text{eff}} > 5 \mu\text{m}$ are found from 150°E to 180°, while the mean D_{eff} remains stable at 4.0 μm throughout eastern NP. To our best knowledge, this study is the first to retrieve both DAOD and coarse-mode dust particle size over global oceans for multiple years. This retrieval dataset provides insightful information for evaluating dust long-wave radiative effects and coarse mode dust particle size in models.

1 Introduction

45 Mineral dust (referred to as “dust”) lifted by strong surface winds in arid and semi-arid regions (Ginoux et al., 2012) is the most abundant type of atmospheric aerosol in terms of dry mass (Kinne et al., 2006; Goudie, 1983). Once aloft, dust particles [with a broad size range \(from 0.001 to 100 \$\mu\text{m}\$ \)](#) can be [transported carried by winds for long-range transport on from local scales to intercontinental and further to hemispherical scales](#), exerting far-reaching impacts on the climate system (Shao et al., 2011; Choobari et al., 2014; Yu et al., 2013; Tegen and Fung, 1994; Uno et al., 2009).
50 For example, dust significantly influences the earth system’s radiative budget by interacting with both shortwave (SW) solar and longwave (LW) terrestrial radiations, known as the direct radiative effects (DRE). Previous studies have found that on a global mean basis, the dust DRE at the top of the atmosphere (TOA) is generally negative in SW (i.e., a cooling effect) but positive (i.e., a warming effect) in LW, although dust SW DRE can be positive over bright surfaces (Kok et al. 2017, Li et al. 2021, Di Biagio et al., 2021, Song et al. 2018, 2022). Despite this qualitative
55 understanding, the quantification of dust net DRE (i.e., SW DRE + LW DRE) remains highly uncertain, in part due to the great spatiotemporal heterogeneity of dust properties such as dust loading, optically represented by dust aerosol optical depth (DAOD) (Huneeus et al., 2011), particle size distribution (PSD) (Kok et al. 2017, Adebisi and Kok, 2020a), particle shape, and refractive indices (RI) (Li et al., 2021). [The dust-radiation interactions perturb the surface energy balance and atmospheric heating rate and hence the thermodynamic structure of the atmosphere \(Helmert et al., 2007\), which in turn affects boundary layer dynamics and cloud formation processes \(Amiri-Farahani et al., 2017; Grogan et al., 2016; Zhang et al., 2007\).](#)
60

Satellite remote sensing is uniquely capable of measuring the spatiotemporal variation of dust properties on regional to global scales and over years and decades. Many methods have been developed to retrieve the column-integrated
65 AOD in the visible spectrum (AOD_{VIS}) (e.g., 550 nm) from passive satellite observations in the visible (VIS) and near-infrared (NIR) spectrum, such as the Moderate Resolution Imaging Spectroradiometer (MODIS) (Levy et al., 2013, Hsu et al., 2013) and the Multi-angle Imaging Spectroradiometer (MISR) (Kahn et al., 2010). It should be noted that these retrievals obtain the total AOD contributed by not only dust but also other types of aerosols. As a result, the fraction of dust AOD (DAOD) in VIS (DAOD_{VIS}) needs to be further separated from the total AOD_{VIS} for dust-focused
70 studies. Some methods rely on model simulations of $\text{DAOD}_{\text{VIS}}/\text{AOD}_{\text{VIS}}$ (Gkikas et al., 2021) or non-dust AOD_{VIS} (Ridley et al., 2016). Others are based on the contrasting properties of dust in comparison with other aerosols, such as its larger size manifested as a smaller Angstrom Exponent and a smaller fine-mode fraction (Kaufman et al., 2005, Yu et al., 2009, 2021) and significant spectral gradient in the absorption from deep blue to the VIS (Ginoux et al., 2010, Pu and Ginoux, 2018). In addition, the active spaceborne Lidars with VIS-NIR channels, such as the Cloud-Aerosol
75 Lidar with Orthogonal Polarization (CALIOP) onboard the Cloud-Aerosol Lidar and Infrared Pathfinder Satellite

Observations (CALIPSO) mission and the Cloud-Aerosol Transport System (CATS), can be used to estimate the vertical distribution of DAOD_{VIS} based on the observed particulate depolarization ratios (Yu et al., 2015b; Proestakis et al., 2018). By utilizing these retrieval methods, several studies further developed decade-long satellite data records of DAOD_{VIS} (Gkikas et al., 2022; Song et al., 2021), which are frequently used for dust studies such as estimations of dust DRE, interannual variability and trends of dust, and global dust cycles (Song et al., 2022; Logothetis et al., 2021; Kok et al., 2021b).

The VIS-NIR dust observations are useful, but they do not provide direct measurements of DAOD at LW and have weak sensitivity to coarse particles ([particle diameter \(\$D_p\$ \) > 1 \$\mu\text{m}\$](#)) (Ryder et al., 2019). Extending observed DAOD from the VIS-NIR to TIR spectra depends strongly on dust PSD and RI assumptions (Song et al., 2018). Therefore, TIR observations are an indispensable complement with several unique advantages. Dust dominated by coarse mode particles is arguably the only predominant particle that can cause strong radiative signatures in the TIR spectrum (Desouza-Machado et al., 2006). Therefore, using TIR observation has an inherent advantage of directly retrieving DAOD, ~~in contrast to the VIS-NIR observations in which empirical methods need to be developed to separate dust without contributions~~ from other ~~types of~~ aerosols. Zheng et al. (2022) showed that direct TIR observations could significantly reduce uncertainties in DAOD_{TIR} and LW DRE associated with dust PSD and RI assumptions. Moreover, previous studies revealed that super-coarse dust particles ($D_p > 20 \mu\text{m}$) are ubiquitously detected from numerous in-situ measurements in both source regions and transport regions (Weinzierl et al., 2017; Denjean et al., 2016; Ryder et al., 2013b; Ryder et al., 2018), which however is excluded or underestimated in most dust transport models (Checa-Garcia et al., 2021; Wu et al., 2020; Zhao et al., 2022). How many and how frequently can super-coarse dust particles be carried in long-range transport? The lack of observational data with finer spatiotemporal coverage prevents us from further revealing their transport patterns. TIR satellite observations with great sensitivity to super coarse particles can potentially fill this knowledge gap.

Notwithstanding the advantages, retrieving dust properties in TIR, particularly the dust particle size, usually represented by effective radius or diameter, is challenging. In the past, TIR dust retrieval algorithms were primarily based on observations from space-borne hyperspectral atmospheric sounders, such as the Advanced Infrared Radiation Sounder (AIRS) and the Infrared Atmospheric Sounding Interferometer (IASI). The important advantages of hyperspectral observations for dust retrieval are that they can provide multiple atmospheric window channels ~~that are~~ most sensitive to dust aerosols ~~with little gas absorption and less sensitive to atmospheric gas absorption~~ (Peyridieu et al., 2010; Capelle et al., 2018; Capelle et al., 2014; Peyridieu et al., 2013). On the other hand, these algorithms have two major limitations. First, the altitude of a dust layer and, therefore, its temperature profile affect the outgoing TIR radiance at TOA with a similar magnitude as DAOD (Pierangelo et al., 2004). As a result, dust altitude must be part of the state vector to be retrieved together with DAOD in a stand-alone hyperspectral TIR dust retrieval algorithm, which makes retrieving dust particle size from limited information contents highly challenging (Pierangelo et al., 2005). Second, the relatively large footprint of hyperspectral sounders (~15 km) makes cloud masking and clearing a daunting task. As a result, the retrieval results are prone to cloud contamination (Song et al. 2018, Zheng et al. 2022).

115 A recent study by Zheng et al. (2022) (hereafter referred to as Z22) opened a new avenue for TIR-based dust retrievals
by retrieving ten years of TIR DAOD at 5-km resolution over the global oceans based on combined CALIOP and
Infrared Imaging Radiometer (IIR, a collocated higher-spatial-resolution TIR imager) observations. Both CALIOP
and IIR are onboard the CALIPSO satellite. The smaller (compared to AIRS and IASI) footprint size of IIR and the
collocated CALIOP lidar make cloud masking much easier and more reliable than stand-alone hyperspectral
120 algorithms. Moreover, the highly detailed and accurate dust vertical distribution provided by CALIOP not only makes
the TIR DAOD retrieval more straightforward and accurate, but also allows for additional retrievals on dust particle
size. Lastly, the collocated CALIOP Lidar also provides estimated $DAOD_{VIS}$, which opens potential applications for
the observational synergistic VIS and TIR DAOD. Furthermore, unlike the passive VIS-NIR observations that are
available at the daytime only, the combined VIS Lidar and TIR observations are also accessible at night, which allows
125 further applications for investigating the diurnal variability of dust properties (Yu, Y. et al., 2021; Chédin et al., 2020).
However, Z22 found that an accurate radiative closure between the simulated TIR radiance and observed TIR radiance
for clear sky backgrounds is only possible for nighttime observations as there is an unresolved bias at daytime. In
addition, because it used a single-band (i.e., the 10.6 μm IIR band) retrieval method, the algorithm allows for retrieving
DAOD only.

130 To overcome the limitations in Z22 and further advance the TIR dust retrievals for coarse-mode dust size, in this
study, instead of IIR, we use three MODIS TIR window bands (centred at 8.55 μm , 11.02 μm and 12.03 μm) for dust
retrievals for the following reasons. The detector noise of MODIS in warm scenes (e.g., dust-laden sky) is 0.02-0.03
K, which is lower than that of IIR at 0.1-0.15 K (Madhavan et al., 2016). As a result, we can achieve a better radiative
closure between radiative transfer simulation and MODIS observations in the clear sky, a premise for TIR-based dust
135 retrieval, at all three TIR channels in both daytime and nighttime (details in Section 2.3). It first allows us to adopt the
split-window technique (Zhang et al., 2006; Paepe and Dewitte, 2009) to reduce retrieval uncertainties compared with
Z22 (detailed in Section 5.1). Moreover, by leveraging the information contents from all three bands, we can retrieve
not only DAOD at 11 μm , further scaled to 10 μm (referred to as “ $DAOD_{10\mu\text{m}}$ ”), but also the dust particle size
represented by effective diameter (referred to as “ D_{eff} ”). Lastly, the daytime retrievals enable comparisons with VIS-
140 NIR-based retrievals, such as MODIS, CALIOP and AERONET.

In the rest of the article, we introduce the collocated MODIS and CALIOP observation and the radiative transfer model
in section 2. The implementation of the retrieval algorithm is detailed in section 3. Section 4 demonstrates the
 $DAOD_{10\mu\text{m}}$ and D_{eff} retrievals of three dust cases observed at Cape Verde and in the Caribbean Sea and compares them
145 with ground-based and in-situ airborne measurements. Section 5 presents the climatological analysis of five-year
retrievals of $DAOD_{10\mu\text{m}}$ compared with Z22 IIR-based and IASI-based retrievals and D_{eff} in terms of the seasonal and
regional variation from 2013 to 2017. The discussions and conclusions are summarized in section 6.

2 Data and model

2.1 MODIS and CALIOP observations

150 In this study, dust properties, namely $DAOD_{10\mu m}$ and D_{eff} , are retrieved from collocated Aqua-MODIS and CALIOP observations. MODIS onboard the Aqua satellite, as a member of the A-train constellation, provides observations from 36 spectral bands ranging from VIS to TIR with near-daily global coverage and relatively high spatial resolution (i.e., 250 m to 1 km at nadir). MODIS is equipped with onboard calibrators that enable stable calibration uncertainties within ± 0.03 K for TIR bands (Xiong et al., 2009). This study primarily uses the MODIS Level-1B calibrated
155 upwelling radiances at TOA at three TIR spectral bands centered at 8.55 μm , 11.02 μm and 12.03 μm , respectively. The TIR “window” bands mostly avoid contaminations from atmospheric gas absorptions and are sensitive to dust optical properties in different orders (Z22). For better interpretation, the calibrated radiances are further converted to equivalent brightness temperature (BT) computed based on Planck’s law, and the corresponding spectral response functions at the three selected TIR bands (see Figure 4b (black dash lines) in Section 3.2).

160 CALIPSO, launched in 2006, has also been a member of the A-train constellation that shares a similar and tightly controlled Sun-synchronous polar orbit with Aqua MODIS until August 2018. CALIOP aboard CALIPSO is a two-wavelength (532 and 1064 nm) polarization-sensitive Lidar with three receiver channels (one measuring the 1064 nm backscatter intensity and two measuring orthogonally polarized components of the 532 nm backscatter). Unlike Aqua
165 MODIS, CALIOP has a much smaller spatial coverage due to its narrow cross-track footprint of around 70 m in diameter. However, the 333-m along-track footprint with 30-to-60-m vertical resolution allows CALIOP to provide detailed vertical structures of aerosols and clouds (Winker et al., 2009).

In this study, the dust contribution to a vertical column of attenuated backscatter is needed as we focus on retrieving
170 dust. Although the CALIOP operational aerosol product (i.e., the Vertical Feature Mask (VFM) product) determines the aerosol sub-type for each aerosol layer (Kim et al., 2018), it does not provide the quantitative dust backscatter profile for dust and non-dust aerosols mixed in the column. Therefore, we apply the estimated particulate depolarization ratio (DPR) profile along with the total attenuated backscatter profile from the Version-4 Level-2 CALIOP aerosol profile product (“LID_L2_05kmAPro-Standard-V4” (Liu et al., 2019)) to derive the dust aerosol’s
175 vertical distribution for $DAOD_{10\mu m}$ and D_{eff} retrieval. The VFM product is further used for filtering out the mis-included non-dust aerosol profiles (see Appendix B for detail).

2.2 AMSR-E and MERRA-2 auxiliary data

The surface characteristics (i.e., surface emissivity and temperature) and the atmospheric profiles (i.e., temperature T, pressure P, water vapor Qv and ozone O₃) are crucial for obtaining an accurate radiative transfer simulation in TIR at
180 TOA (Scott and Chedin, 1981). Unlike the hyperspectral observations with the capability to retrieve the instantaneous atmospheric states, our retrieval requires inputs of these auxiliary data from third-party sources.

The atmospheric profiles T, P, Qv and O₃, are obtained from Version 2 Modern-Era Retrospective analysis for Research and Applications (MERRA-2) assimilated products (Gelaro et al., 2017). Specifically, The MERRA-2 “inst3_3d_asm_Nv” product provides 3-hourly instantaneous atmospheric profiles at 72 pressure levels with a gridded horizontal resolution of 0.625° longitude by 0.5° latitude. Detailed information can be found in Gelaro et al. (2017). To assign the gridded MERRA-2 data to the simulations for the collocated MODIS and CALIOP (referred to as “MODIS-CALIOP”) observations, we first obtain the geolocation and time of all grid cells of MERRA-2 data. Then, we find the spatially and temporally closest grid cell with each MODIS-CALIOP pixel.

As the retrieval is implemented over oceans only, which is explained in Section 2.3, we obtain the level-2 sea surface temperature (SST) retrieved based on the Advanced Microwave Scanning Radiometer - Earth Observing System Sensor (AMSR-E) onboard Aqua (ceased operation in December 2011), and its successor (launched in May 2012), the Advanced Microwave Scanning Radiometer 2 (AMSR2) onboard GCOM-W1 that follows Aqua’s orbit. The 6.9-GHz and 10.7-GHz channels from AMSR-E and AMSR2 are used for SST retrieval (Wentz and Meissner, 2000). Previous studies demonstrated that the SST retrievals over heavy dust-loading regions using TIR observations are underestimated due to the radiative impact of dust (Luo et al., 2019). However, microwave radiation has mostly no interaction with dust and, therefore, can avoid dust impacts and achieve better SST retrieval accuracy over dusty regions (O’carroll et al., 2019). In this study, the SST at 56 km resolution from AMSR-E and AMSR-2 is collocated with MODIS-CALIOP. [Specifically, the SST from AMSR-E and AMSR2 are used for retrievals before August 2011 and after June 2012, respectively, while there will be no retrievals during the observational gap between ASMR-E and ASMR2.](#) For the surface emissivity, we use the emissivity models (listed in Table 1) provided in version-2 Community Radiative Transfer Model (CRTM) (Van Delst, 2011), which is described in Section 2.3.

Finally, for each MODIS-CALIOP observation, the collocated MERRA-2 atmospheric profiles, AMSR-E/AMSR2 SST, and the internal surface emissivity model are used as the input for the radiative transfer simulation. All the satellite products, variables and auxiliary data are listed in Table 1.

Table 1: Values of variables from multi-source satellite sensors and auxiliary datasets that are used in this study

Satellite sensors	Product names	Variable names	Value is used
MODIS	MYD021KM (CloudSat_MODIS_AUX)	EV_1KM_Emissive	Radiances (BTs) at 8.5 μm, 11 μm, 12 μm
	MYD06 (CloudSat_MOD06_AUX)	Cloud_Phase_Optical_Properties (For daytime)	Clear (0)
		Viewing zenith angle	All
CALIOP		CAD_score	-100 to -90
	LID_L2_05kmAPro-Standard-V4-20	Particulate_Depolarization_Ratio_Profile_532	All
		Extinction_QC_Flag_532	0,1,16,18
		Total_Backscatter_Coefficient_532	All

		Atmospheric_Volume_Description	Three dust subtypes (dust, polluted dust, dusty marine)
	CAL_IIR_L2_Track-Standard- V4-20	Was_Cleared_Flag_1km	No single-shot cloud (0)
		TGeotype	Open Water (1700)
AMSR-E	AMSR_E_L2_Ocean	SST (sea surface temperature)	All
AMSR2	RSS_AMSR2_ocean_L3_daily		
Auxiliary data	Product names	Variable names	Value is used
MERRA-2	Inst3_3d_asm_Nv	H, P, T, QV, O3	All
CRTMv2.3	Nalli.IRwater.EmisCoeff	Surface emissivity	All

210

2.3 The radiative transfer models

The foundation of a LUT-based retrieval method is an accurate radiative transfer model. For the radiative transfer simulation of terrestrial TIR radiation under clear atmospheric conditions, atmospheric gaseous absorption is critical. In this study, we use the version-2 CRTM developed by the US Joint Center for satellite data Assimilation (JCSDA) as the foothold for our retrieval (Chen et al., 2012; Han, 2006). The transmittance coefficients in CRTM are first trained by applying regression algorithms to the line-by-line integrated transmittances for numerous atmospheric profiles (McMillin et al., 2006). Afterward, the gaseous absorption component can achieve an accuracy as high as the line-by-line transmittance but consumes far less computational time (Ding et al., 2011). As CRTM also supports MODIS's sensor coefficients, it is an optimal tool for simulating the atmospheric gaseous absorptions at the three selected MODIS TIR bands for our retrieval (Liang et al., 2016; Wang et al., 2016).

215

220

Although it is straightforward to use CRTM to handle the gas absorptions in the TIR, we found it difficult to use it to handle the scattering and absorption of dust due to the configuration and structure of the code. In this study, we use the Discrete Ordinate Radiative Transfer code (DISORT) to handle the dust aerosol scattering and absorption calculation (Stamnes et al., 1988). To combine CRTM and DISORT, we first use CRTM to simulate atmospheric gaseous absorptions (output as the atmospheric optical depth) with input MERRA-2 atmospheric profiles. Afterward, the CRTM-simulated atmospheric optical depth with and without the vertical distribution of dust optical properties served as inputs for DISORT to simulate cloud-free dust-laden BTs and cloud-free clean (i.e., cloud-free and aerosol-free) BTs at the three MODIS TIR bands at TOA, respectively.

225

230

Prior to implementing the retrieval, the uncertainties contributed by the auxiliary data, the radiative transfer simulation, and the observational errors must be evaluated. Thus, we conduct the radiative closure benchmark between the CRTM-DISORT calculated and the MODIS-observed BTs under cloud-free and clean (without dust) conditions, which is detailedly presented in Appendix A. Given that the error of the radiative closure benchmark over land and polar regions

235 can reach up to 10 K due to the uncertainties from the assumed surface emissivity and temperatures (Z22), this study
focuses on retrievals over oceans within 60°S and 60°N only.

3 Description of the retrieval algorithm

240 In this section, we detail describe the retrieval algorithm that is summarized in Figure 1, covering the collocation of
MODIS and CALIOP observations and the process of cloud masking and dust detection, the *a priori* dust properties,
and the design of the LUT method and the uncertainty estimation.

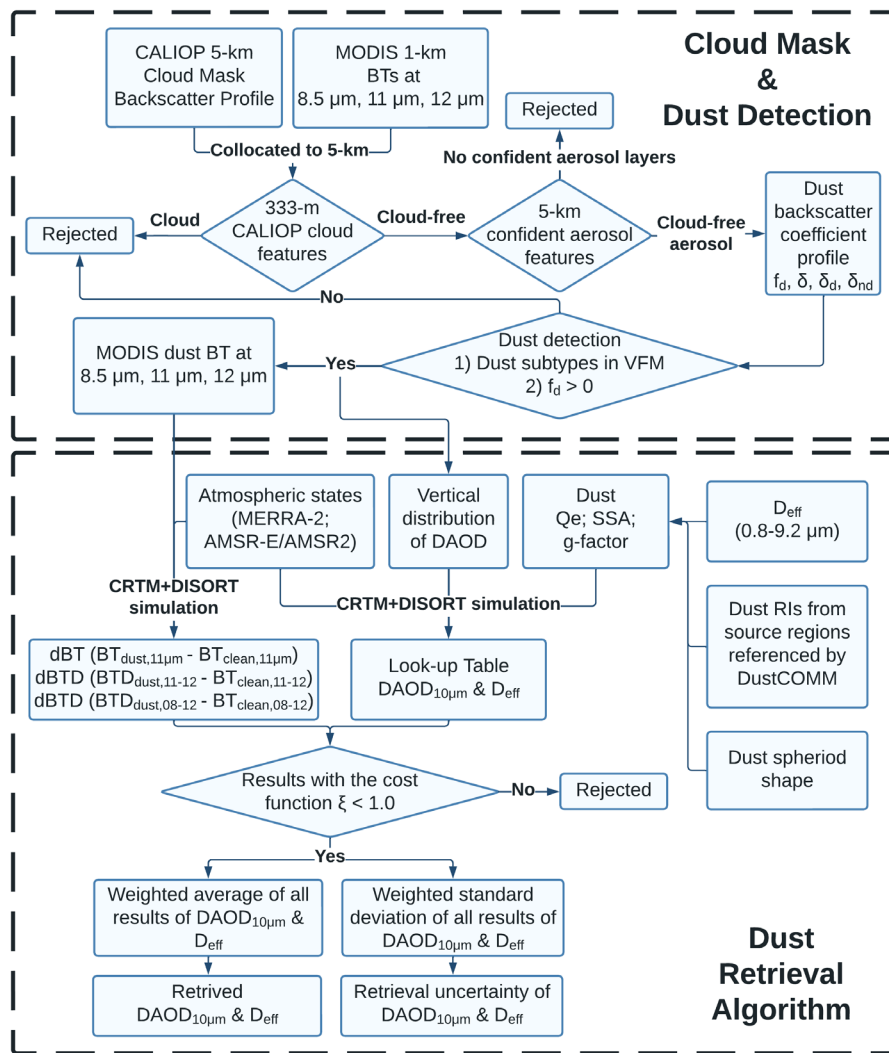


Figure 1: The flow chart of the retrieval process of DAOD_{10µm} and D_{eff} using collocated MODIS-CALIOP observations.

245 The first step of the retrieval is to identify high-quality cloud-free dust-laden observations. Due to the different spatial coverage of MODIS and CALIOP, the retrieval requires collocated data from both sensors. The collocation process and the following cloud masking and dust detection and vertical distribution processing are similar to Z22 and are presented in detail in Appendix B. [It should be noted that CALIOP has relatively smaller signal-to-noise ratios during](#)

250 [daytime than nighttime, owing to the influence of solar contamination on the Lidar signal \(Megill-McGill et al., 2007\). Nevertheless, by applying identical selection criteria for high-quality cloud-free dust vertical profiles in both daytime and nighttime, we can ensure that the data quality of the selected CALIOP cloud-free dust profiles remains consistent across both periods.](#)

3.1 *A priori* dust properties

265 In addition to the vertical distribution, the retrieval needs to assume dust bulk optical properties. In this section, we introduce the dust PSD, dust shapes, and dust RI that are used to calculate the bulk optical properties (i.e., the extinction efficiency (Q_{ext}), single scattering albedo (SSA) and asymmetry factor (g-factor)).

3.1.1 Monomodal dust coarse-mode particle size distribution

260 Dust PSD is commonly presented by a two-mode (i.e., fine mode ($D_p < 1.0 \mu\text{m}$) and coarse mode ($D_p > 1.0 \mu\text{m}$)) lognormal size distribution (Dubovik et al., 2002). As the fine mode dust has a negligible effect on TIR observation, we assume a normalized (i.e., total volume concentration equals unity) monomodal lognormal volume size distribution to represent the coarse-mode dust PSD, which is defined as

$$\frac{dV}{d \ln D} = \frac{1}{\sqrt{2\pi}\sigma} \exp\left[-\frac{\ln^2(D/D_m)}{2\sigma^2}\right] \quad (1)$$

265 where D is the volume-equivalent sphere geometric diameter for spheroidal dust particle assumption (see Section 3.1.2), D_m is the geometric volume median diameter, $\frac{dV}{d \ln D}$ is the volume PSD, and σ is the standard deviation. Note that the sensitivity of σ to the TIR radiative signature at TOA is negligible compared with that of AOD and D_m (Pierangelo et al., 2005) (see Figure S5). Therefore, to simplify the retrieval, we first set $\sigma = 0.7$ (i.e., $\ln(2.0)$) as it is a good representation for the coarse-mode dust PSDs in both in-situ measurements and satellite retrievals (Capelle et al., 2018; Ryder et al., 2018). We further use the effective diameter defined by Hansen and Travis (1974) to represent the monomodal PSDs with dependence on D_m as

$$D_{\text{eff}} = \frac{\int_0^\infty D^3 n(D) dD}{\int_0^\infty D^2 n(D) dD} \quad (2)$$

270 where $n(D)$ is the dust number concentration converted by the volume distribution with $\sigma = 0.7$ and varied D_m .

275 Note that in-situ measurements of dust PSD show that the coarsest record of dust particles over the transport regions (i.e., over oceans) was measured during the Fennec campaign in June 2011 (Ryder et al., 2013a), with an estimated D_m at around $10.0 \mu\text{m}$. Therefore, for the retrieval, we define the minimum and maximum dust coarse-mode PSDs with their representations of D_m from $1 \mu\text{m}$ to $12 \mu\text{m}$ and D_{eff} from $0.8 \mu\text{m}$ to $9.2 \mu\text{m}$, (see Figure S1). Dust PSDs within this range are used for calculating the dust bulk optical properties as inputs for building the LUT of $\text{DAOD}_{10\mu\text{m}}$ and D_{eff} .

3.1.2 Dust refractive indices and dust shape

280 The RI of dust, determined by dust mineral compositions, has a profound impact on dust scattering properties and therefore the retrieval results (Sokolik and Toon, 1999). Ideally, the dust RI should be retrieved simultaneously with

Formatted: English (United States)

other properties of dust. However, given the highly limited information content from the three MODIS TIR bands, a retrieval of dust RI is not possible, at least in this study. It should be noted that most previous studies also used pre-assumed dust RI, often one or two simple global constants, in their retrievals including widely used operational aerosol retrieval products (Capelle et al., 2018; Zhou et al., 2020).

Nevertheless, in this study, we try to incorporate the spatial variability of dust RI in our retrieval by using two newly developed datasets. One is a state-of-the-art dust RI database developed by Di Biagio et al. (2017) (referred to as the “Di-Biagio RI”), which provides dust RIs retrieved based on surface soil samples collected in nineteen arid and semi-arid sites from worldwide dust source regions. The Di-Biagio RI database provides the observational basis for accounting for the regional dependence of dust RI. The other is the fractional contribution over oceans supplied by various dust source regions from the DustCOMM-2021 dataset developed by Kok et al. (2021a), which is used to assign dust RIs from different source regions to the observed dust aerosol over oceans. Details of the dust RI assignments are presented in Appendix C.

Dust particles have irregular and non-spherical shapes, which vary greatly from case to case and from location to location (Scheuven and Kandler, 2014). Using spherical assumptions for non-spherical dust in remote sensing would cause significant uncertainty (Huang et al., 2020; Dubovik et al., 2002; Nousiainen and Kandler, 2015). It is essential to adopt a quantified non-sphericity to represent dust optical properties better. However, characterizing the complex morphology of dust particles remains challenging. Previous studies used different assumptions of dust particle shape to evaluate the sensitivity of dust optical properties to the morphology, such as spheroid (Dubovik et al., 2006), ellipsoid (Meng et al., 2010) and polyhedral (Liu et al., 2013).

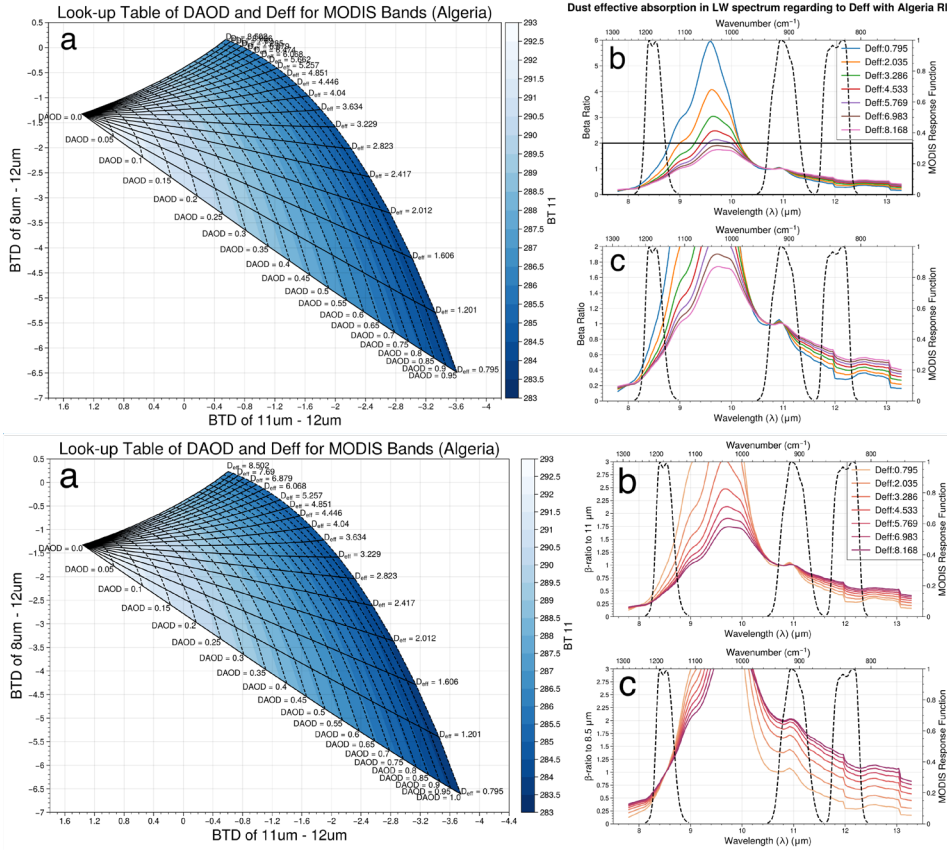
The non-sphericity of the aspherical shape is often represented by the aspect ratio, defined as the ratio of the longest particle dimension to the intermediate particle dimension. The higher the aspect ratio, the greater the non-sphericity. The spheroid shape assumption is a first-order approximation of dust non-sphericity (Mishchenko et al., 1997; Dubovik et al., 2002) and is widely used for non-spherical aerosol retrievals (Levy et al., 2013; Kahn et al., 2010). To seek a broader application of this study to others, we stick to the spheroid assumption with the size-independent aspect ratio distribution from Dubovik et al. (2006) for the retrieval. Nonetheless, the retrieval based on a more advanced non-spherical dust optical properties database, such as the hexahedral shape (Saito et al., 2021), will be evaluated in future studies.

By assuming dust particles with spheroidal shape, we calculate the dust single-particle optical properties for each *a priori* dust RI using the T-matrix method (Mishchenko et al., 1996). Afterward, the bulk optical properties are integrated according to the pre-assumed dust PSDs and [the spheroidal dust aspect ratio distributions of spheroidal dust](#).

3.2 The look-up table and the uncertainty estimation

320 The $DAOD_{10\mu m}$ and D_{eff} are retrieved from three MODIS TIR bands using a LUT method. To illustrate the LUT, we use CRTM-DISORT to simulate the cloud-free clean BT at 11 μm (referred to as “BT₁₁”), spectral BT differences (BTD) between 11 μm and 12 μm (referred to as “BTD₁₁₋₁₂”) and that between 8.5 μm and 12 μm (referred to as “BTD₀₈₋₁₂”), by giving a typical tropical atmospheric profile with a dust layer distributed at the mid-level troposphere (i.e., 2-6 km, see Figure S6). Afterward, with the *a priori* dust D_{eff} , dust RI, and dust spheroidal aspect ratios, the calculated dust bulk optical properties based on the T-matrix method can be used as inputs in CRTM-DISORT to simulate cloud-free dust BT₁₁, BTD₁₁₋₁₂ and BTD₀₈₋₁₂. With the input DAOD at 11 μm ($DAOD_{11\mu m}$) ranging from 0.0
325 to 1.0 and D_{eff} ranging from 0.8 μm to 9.2 μm (see Figure S1 for corresponding dust PSDs), we build a LUT consisting of BT₁₁, BTD₈₋₁₂ and BTD₁₁₋₁₂ as shown in Figure 2a. The assumed dust RI for the LUT is from Algeria in Northeast Africa. Example LUTs corresponding to other dust RIs are shown in Figures S7 and S8.

330 Considering the higher dust extinction signal expected at 10 μm compared to 11 μm (see Figure 2b and Pierangelo et al. (2004)), we scale $DAOD_{11\mu m}$ to $DAOD_{10\mu m}$ based on the Q_e spectral behavior following $\frac{DAOD_{11\mu m}}{DAOD_{10\mu m}} = \frac{Q_{e11\mu m}}{Q_{e10\mu m}}$. As a result, our final retrieval products contain $DAOD_{10\mu m}$ and D_{eff} .



335 **Figure 2: (a) The example of the LUT of BT_{D8-12} (y-axis), BT_{D11-12} (x-axis) and BT₁₁ (colour-filled contours) corresponding to DAOD_{11μm} ranging from 0.0 to 1.0 (dashed lines) and D_{eff} ranging from 0.8 μm to 8.2 μm (solid lines) and the Algeria dust RI from Di-Biagio Database. At the point of DAOD = 0.0, the BT_{D8-12} and BT_{D11-12} correspond to the cloud-free clean scenario. (b) The β-ratio to 11 μm calculated based on D_{eff} ranging from 0.8 μm to 8.2 μm and the Algeria dust RI within the TIR spectrum between 7.5 μm and 13.5 μm. (c) Same as (b) but the β-ratio to 8.5 μm. The zoom-in area of the black rectangle in (b).**

340

The variation of BTDs and BT₁₁ with DAOD_{11μm} and D_{eff} is determined by the dust Q_e, SSA and g-factor at the three TIR bands. To better understand the variations of BTDs in the LUT, we introduce the so-called β-ratio, defined as follows.

345

$$\beta(\lambda_1/\lambda_2) = \frac{Q_e(\lambda_1)[1-\omega(\lambda_1)g(\lambda_1)]}{Q_e(\lambda_2)[1-\omega(\lambda_2)g(\lambda_2)]} \quad (3)$$

where Q_e is the extinction efficiency, ω is the SSA, and g is the asymmetry factor. The β-ratio was often used to represent the spectral difference of dust “effective absorption” (i.e., absorption and backward scattering) in the TIR spectrum in many studies on dust, volcanic ash and ice cloud retrieval (Pavolonis et al., 2013; Pavolonis et al., 2015; Garnier et al., 2013). Because the variation of BT₁₁ in Figure 2a serves as the single-band dust radiative signature, we

350 present the β -ratio with respect to 11 μm (i.e., $\lambda_2 = 11 \mu\text{m}$ in Eq.(3)) for varied D_{eff} , as shown in Figure 2b. The β -
 ratios for wavelength ranging from 12 μm to 11 μm over the whole range of the input D_{eff} are lower than one. It means
 that the dust “effective absorption” at 11 μm is always more significant than that at 12 μm , regardless of the size
 variation. In contrast, the cloud-free clean BT at 11 μm is higher than that at 12 μm due to the less atmospheric
 absorptions at 11 μm as described in Appendix A. Consequently, in Figure 2a, the BTD_{11-12} decreases with increasing
 355 $\text{DAOD}_{11\mu\text{m}}$ regardless of how D_{eff} changes.

On the other hand, the BTD_{8-12} is more sensitive to D_{eff} than to DAOD . First, the cloud-free and clean BT at 8.5 μm
 is similar to that at 12 μm due to similar gas absorption. However, the dust “effective absorption” at 8.5 μm is larger
 than that at 12 μm when D_{eff} is relatively small (e.g., $1.0 \mu\text{m} < D_{\text{eff}} < 3.03.2 \mu\text{m}$) in Figure 2b2c, there are negative
 360 trends of BTD_{8-12} with increasing DAOD in Figure 2a. In contrast, in Figure 2b2c, the dust “effective absorption” at
 8.5 μm is weaker than that at 12 μm when D_{eff} is relatively large (e.g., $D_{\text{eff}} > 5.04.5 \mu\text{m}$), leading to positive trends of
 BTD_{8-12} with increasing DAOD in Figure 2a. In between, the sensitivity of BTD_{8-12} to DAOD can be nearly zero when
 dust D_{eff} is moderate (e.g., $D_{\text{eff}} = 3.6 \mu\text{m}$ in Figure 2a). As such, the radiative signature of DAOD and D_{eff} can be
 separated using BTD_{8-12} and BTD_{11-12} , allowing the simultaneous retrieval of both parameters based on the three
 365 MODIS TIR bands.

Besides the dust particle size (e.g., D_{eff}), dust “effective absorption” at the three TIR bands also depends on the LW
 dust RI, especially the β -ratio from 12 μm to 8.5 μm (see Figure S7). The dust RI directly changes the spectral
 behavior of the dust “effective absorption” and reshapes the LUT of BTD_{8-12} and BTD_{11-12} (see Figures S7-S8 and
 370 S8S9). Due to the limited observational signature, the retrieval of dust RI is unachievable in this study. The retrieval
 uncertainty associated with the assumption of dust RI thus needs to be assessed. In addition, the errors resulting from
 radiance observation itself and radiative transfer modeling (Figure A1 in Appendix A) also need to be factored in.

We implement the retrieval algorithm in three steps to find an optimal retrieval with the assessed uncertainties. Firstly,
 375 we define a cost function ξ of the normalized distance between the simulated BT and BTs in the LUT and the
 observed BT and BTs as

$$\xi(\text{DAOD}, D_{\text{eff}}) = \frac{1}{3} \left[\frac{(\text{BT}_{11}^{\text{sim}} - \text{BT}_{11}^{\text{obs}})^2}{\sigma_{11}^2} + \frac{(\text{BTD}_{11-12}^{\text{sim}} - \text{BTD}_{11-12}^{\text{obs}})^2}{\sigma_{11-12}^2} + \frac{(\text{BTD}_{8-12}^{\text{sim}} - \text{BTD}_{8-12}^{\text{obs}})^2}{\sigma_{8-12}^2} \right] \quad (4)$$

The subscript of 11, 11-12 and 8-12 represents the BT at the 11 μm band, BTD_{11-12} and BTD_{8-12} , respectively. The
 superscript of *sim* and *obs* represents the BT or BTD obtained by simulations and observations, respectively. The σ
 380 represents the standard deviation of the uncertainty assessed through the clear-sky radiative closure (see Figure A1),
 which represents the summation of errors from the observation and simulation using *a priori* atmosphere states. The
 first term on the right-hand-side of Eq. (4) represents the normalized distance between the observed and the simulated
 BT at the 11 μm band. The second and the last term represents the summation of the normalized distance between the
 observed and the simulated BTD_{11-12} and BTD_{8-12} , respectively.

385

Secondly, by using Eq. (4), we acquire a solution when the normalized distance is within the range of the evaluated uncertainty ($\xi < 1$). In addition, as mentioned in Appendix C, each observation would possibly assume more than one dust RI for retrieval. Therefore, we build multiple LUTs corresponding to multiple RIs and implement the retrieval with all of them. All the solutions that satisfy $\xi < 1$ in these LUTs are collected.

390

Finally, the optimal retrieval results of DAOD and D_{eff} are defined as the average of the collected solutions corresponding to multiple *a priori* dust RIs weighted by their corresponding cost function ξ as $w = 1 - \xi$. The weighted standard deviation thus represents the estimated retrieval uncertainty as

$$S_w = \sqrt{\frac{\sum_{i=1}^N w_i (x_i - \bar{x}_w)^2}{(N-1) \frac{\sum_{i=1}^N w_i}{N}}} \quad (5)$$

395 where x_i is the i^{th} solution of DAOD or D_{eff} , w_i is the weight of ξ for the i^{th} solution, N is the number of non-zero weights, and \bar{x}_w is the weighted mean of the collected solutions (Heckert and Filliben, 2003; Hao and Mendel, 2013). In this step, the uncertainties associated with the assumptions of *a priori* dust RI and the clear-sky radiative closure are taken into account by the weighted average and the weighted standard deviation.

400 After the retrieval, the quality assurance (QA) flag is assigned as 0 for successfully retrieved results. The retrieval with less than two solutions satisfying $\xi < 1$ is rejected and is assigned with QA flag as 1. By implementing the retrieval for the five-year MODIS-CALIOP observations from 2013 to 2017, which will be analyzed in detail in Section 5, we present the seasonal distribution of cloud-free dust samples (N_{dust}), successfully retrieved dust samples ($N_{\text{retrieval}}$; QA flag = 0), and the retrieval success rate ($N_{\text{retrieval}} / N_{\text{dust}}$), which reaches to 90%-100% over dust transport regions, as shown in Figure S109.

405

In summary (Figure 1), we obtain the cloud-free dust aerosol vertical profiles using the CALIOP cloud mask, dust detection and vertical-scaling method introduced in Appendix B. Afterward, the *a priori* dust properties presented in Section 3.1 serve as inputs for CRTM-DISORT to build the LUT of DAOD and D_{eff} . Lastly, we retrieve $\text{DAOD}_{11\mu\text{m}}$ further scaled to $\text{DAOD}_{10\mu\text{m}}$ and D_{eff} by averaging the solutions that satisfy $\xi < 1$ weighted by ξ and estimate the corresponding retrieval uncertainty based on the corresponding ξ -weighted standard deviation. [Both the column integrated \$\text{DAOD}_{10\mu\text{m}}\$ and the vertically resolved extinction coefficients at \$10 \mu\text{m}\$ inferred by the CALIOP dust vertical distribution are provided in our retrieval.](#)

410

415 4 Evaluation of CALIOP-MODIS retrievals with in-situ measurements – case studies

[In this section, we evaluate the retrieval, especially \$D_{\text{eff}}\$, by comparing it with the in-situ measured dust PSDs through case studies. In recent decades, most dust-aerosol-focused field campaigns have taken place in North Africa and North Atlantic, while there are limited in-situ measurements of dust PSD over the Indian Ocean and North Pacific \(Li et al., 2000; Quinn et al., 2002; Clarke et al., 2004\), which all took place before the launch of CALIOP in June 2006. Additionally, due to the narrow spatial coverage of CALIOP orbit tracks \(i.e., 70 m cross-track footprint\) \(Winker et](#)

420

Formatted: Normal

al., 2010). it is difficult to find cases that our retrievals can be well-located with the North Pacific in-situ measurements in space and time. Consequently, in this study, we compare the dust PSDs corresponding to the retrieved D_{eff} with the in-situ measured dust PSDs over the North Atlantic.

4.1 A case study for transported Saharan dusts over Cape Verde in summer

425 In this section First of all, we implemented the retrieval to-on a dust plume originating from North Africa and being transported over the North Atlantic on August 16th, 2015. We use this case to evaluate the retrieved DAOD_{10μm} and D_{eff} through comparisons with the in-situ measured dust particle size and the collocated AERONET (Aerosol Robotic NETwork) version 3 measurements (Holben et al., 1998; Dubovik et al., 2000; Dubovik et al., 2006; Giles et al., 2019).

430 4.1.1 Evaluation of retrieved DAOD_{10μm}

Figure 3a shows the total attenuated backscatter at 532 nm from CALIOP for the dust case observed on August 16th, as shown from left (South) to right (North) with the geolocation highlighted in the upper left sub-panel. The CALIOP orbit passed nearby Cape Verde (16.733°N, 22.935°W) around 03:34 UTC with nighttime observations for the dust plume. Figure 3b shows the corresponding spatial variation of total AOD_{532nm} (blue dots) and DAOD_{532nm} (red dots) estimated with a Lidar ratio of 44 sr and uncertainty of ± 10 sr as described in Appendix B. The mean DAOD_{532nm} (1.1) is $\sim 83\%$ to the mean total AOD_{532nm} (1.33), indicating that “pure” dust aerosols dominate this offshore dust plume. Therefore, as a “golden standard”, the measured AERONET AOD at Cape Verde for this dust plume can be approximated as DAOD to assess the CALIOP DAOD and the corresponding retrieved DAOD_{10μm}. Unfortunately, although AERONET at Cape Verde observed a maximum AOD event at 18:10 on Aug 16th as shown in Figure 3d, it does not provide any nighttime measurement for this case.

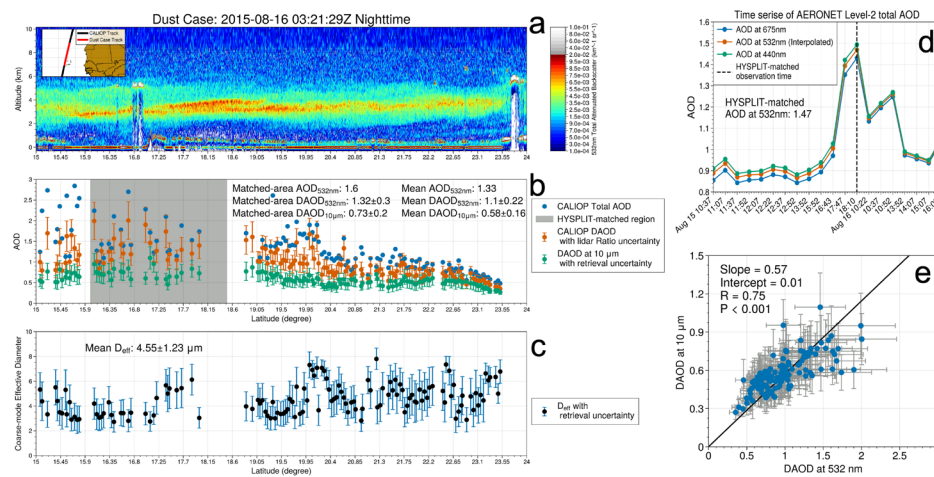
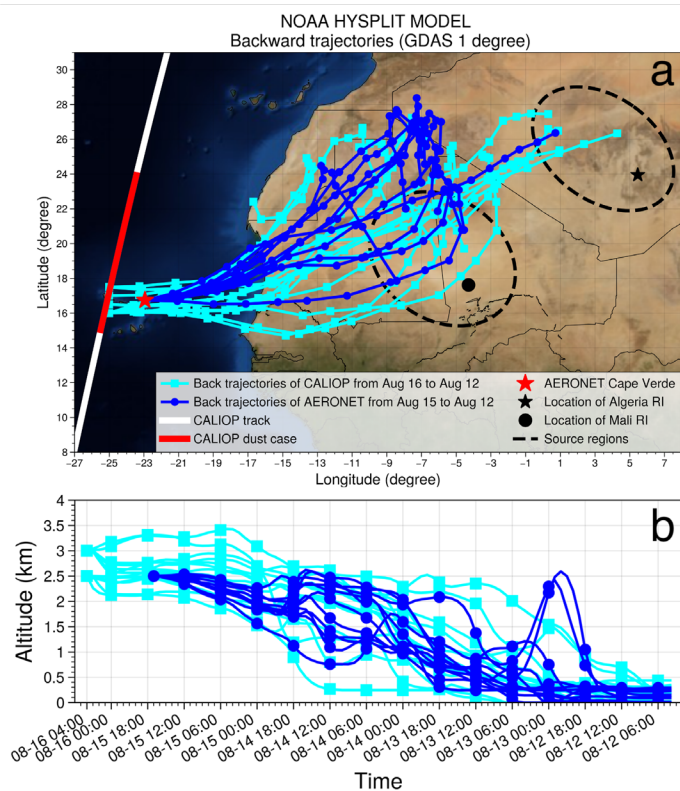


Figure 3: The nighttime case on August 16th, 2015. (a) The CALIOP total attenuated backscatter at 532 nm on August 16th, 2015, over the downwind region of the Sahara Desert (the orbit at upper left). (b) The CALIOP total AOD (blue dots), CALIOP DAOD (red dots), and the retrieved DAOD_{10µm} (green dots) of the cloud-free dust-laden profiles. The gray shadow area represents the part of the dust plume (16°N-18°N) observed by CALIOP that is matched with the AERONET measurement based on the HYSPLIT back trajectories as shown in Figure 4 (c) The retrieved D_{eff} (black dots) of the cloud-free dust-laden profiles with the estimated uncertainty (cyan error bars). (d) The time series of the AERONET level-2 AOD at 675 nm (blue dot line), 440 nm (green dot line) and 532 nm (orange dot line, interpolated) at AERONET Cape Verde from 08-15-2015 to 08-16-2015. The black dash lines indicate the time that AERONET measured the same dust plume observed by CALIOP later, proven by the HYSPLIT back trajectories as shown in Figure 4. (e) The scatter plot of DAOD_{10µm} versus DAOD_{532nm} for the whole dust case. The grey error bars represent the uncertainties of DAOD_{10µm} (vertical) and DAOD_{532nm} (horizontal). The black line represents the robust linear regression with correlation coefficient (R), slope, intercepts, and p-value (P).

Due to the different observation times and locations between CALIOP and AERONET, to compare their AODs, we present the ensemble back trajectories simulated by the Hybrid Single-Particle Lagrangian Integrated Trajectory (HYSPLIT) model (Stein et al., 2015) from the passing-by times of the MODIS-CALIOP orbits and the AERONET Cape Verde as shown in Figure 4. Note that the vertical distribution of the dust plume is concentrated around 3-2 km to 4 km (see Figure 3a). Therefore, the HYSPLIT back trajectories are initiated at 3-2.5 km and 4-3 km. In Figure 4a, the HYSPLIT back trajectories of CALIOP between 16°N to 18°N show that the dust plume was seen by AERONET Cape Verde at 18:10 on Aug 15th (see Figure 4b). Bearing in mind that the AOD of the dust plume may change after the 10-hour transport from AERONET Cape Verde to the CALIOP orbit track, we found that the CALIOP DAOD_{532nm} (1.32 ± 0.3 averaged from 16°N to 18°N, Figure 3b) is consistent with the AERONET AOD_{532nm} (interpolated, Figure 3d) of 1.47 within its uncertainty.

In addition, both back trajectories from CALIOP (including trajectories > 18°N) and AERONET show similar transport patterns from east to west with initial emission (i.e., back trajectories' height reaches 0 km in Figure 4b) from the source regions (black dash regions in Figure 4a) in Algeria and Mali in both horizontal and vertical view. Thus, we can assign the Di-Biagio RIs from Algeria and Mali as the *a priori* dust RI for retrieval. The retrieved DAOD_{10µm} (green dots in Figure 3b) shows a reasonable correlation with DAOD_{532nm} ($R = 0.75$ in Figure 3e). Because of the spectral difference between TIR and VIS, the HYSPLIT-matched mean DAOD_{10µm} (0.73) is ~55% of the value of DAOD_{532nm} (1.32). For the entire case, DAOD_{10µm} is ~57% ($k = 0.57$ in Figure 3e) of DAOD_{532nm}. Note that both ratios are within the empirical range of the TIR-to-VIS DAOD ratio from 28% to 65% (Peyridieu et al., 2013), depending on the assumptions of dust PSD, dust RI and dust non-spherical shape.

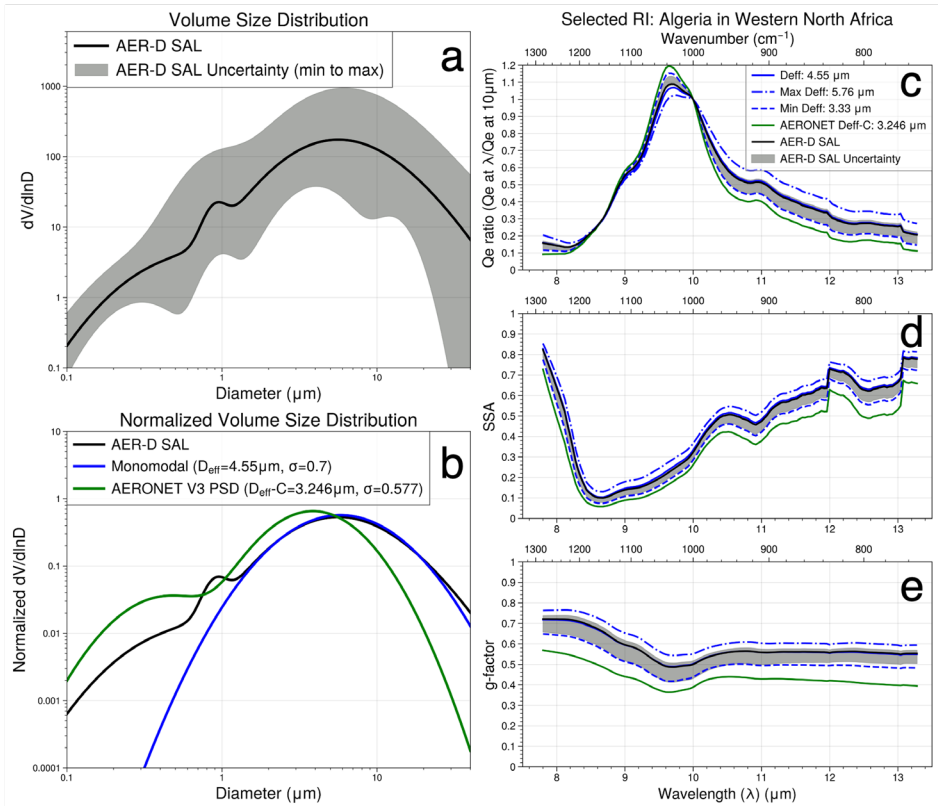


480 **Figure 4:** The distribution of the spatial (a) and the vertical (b) ensemble HYSPLIT back trajectories on the CALIOP dust case on 08-16-2015 (cyan rectangle solid lines) and the AERONET Cape Verde observation for the dust case on 08-15-2015 (blue dot solid lines). The black star and circle represent the geolocation of Di-Biagio RI collected over Algeria and Mali, respectively. The red star denotes the geolocation of the AERONET Cape Verde site.

4.1.2 Comparison of D_{eff} with AER-D in-situ measurements

485 In this section, we evaluate the D_{eff} retrieval by comparing the D_{eff} -corresponding monomodal PSD with those deduced from the lognormal-fitted dust PSD measured during the AERosol Properties – Dust (AER-D) campaign from Aug 7th to Aug 25th, 2015, over the outflow region of North Africa around Cape Verde (Ryder et al., 2018). We also compared with the AERONET-version-3 Level-2 two-mode PSD (referred to as “AERONET PSD”) on Aug 16th at Cape Verde (Dubovik et al., 2006) (see Figure 5b). The AER-D campaign provides measured dust PSD and the corresponding uncertainty for dust within the Sahara Air Layer (SAL) (see Figure 5a) and in the marine boundary layer from various airborne instruments (Ryder et al., 2018). In this case, as the CALIOP-observed dust plume is well

490 confined within 2-5 km (Figure 3a), we choose the AER-D SAL campaign mean log-fit size distribution (referred to as “AER-D PSD”), which is measured within 1.2-4.8 km (Ryder et al., 2018), in our comparison.



495 **Figure 5: (a) The volume lognormal ($dV/d\ln D$) AER-D PSD (black) with gray shadow area indicating the min-to-max range of the measurement uncertainty obtained from Ryder et al. (2018). (b) The normalized $dV/d\ln D$ of AER-D (black), the retrieved coarse mode PSD corresponding to $D_{\text{eff}} = 4.55 \mu\text{m}$ (blue) and the AERONET PSD (green). (c-e) The Q_e ratio to $10 \mu\text{m}$ (c), SSA (d), g-factor (e) calculated based on the AER-D PSD (black) with min-to-max uncertainty (grey shadow), retrieved coarse mode PSD (blue) with the retrieval uncertainty (blue dash curve for the lower bound; blue dash-dot curve for the upper bound) and AERONET PSD (green).**

500 Figure 3c shows the retrieved D_{eff} for the dust case. We found that the spatial variation of D_{eff} is generally positively correlated with that of $DAOD_{10\mu\text{m}}$ and with a mean value of $4.55 \mu\text{m}$ with the uncertainty ranging from $3.33 \mu\text{m}$ to $5.76 \mu\text{m}$. Therefore, we obtain the monomodal PSD corresponding to $D_{\text{eff}} = 4.55 \mu\text{m}$ to compare with the normalized AER-D PSD and the AERONET PSD. In Figure 5b, the AERONET-retrieved coarse mode PSD is systematically

505 smaller than that of AER-D, while the monomodal PSD with $D_{\text{eff}} = 4.55 \mu\text{m}$ agrees well with the AER-D coarse mode
PSD, although the fine mode of AER-D PSD is not compared because not relevant for LW.

For a perhaps more relevant comparison of the three PSDs in coarse mode, we compare their corresponding optical
properties, namely the dust Qe ratio at $10\mu\text{m}$, SSA and g-factor in the TIR spectrum ranging from $8 \mu\text{m}$ to $13 \mu\text{m}$ (See
510 Figures 5c to 5e). The reason for using the dust Qe ratio at $10 \mu\text{m}$ is that the retrieved $\text{DAOD}_{10\mu\text{m}}$ provides a constraint
of dust extinction at $10 \mu\text{m}$, while the dust PSD further determines the spectral Qe ratio of other TIR wavelength to
 $10 \mu\text{m}$. We found that the spectral Qe ratio, SSA and g-factor calculated based on the monomodal PSD used in our
retrievals are consistent with that calculated based on AER-D PSD. It demonstrates that although our monomodal PSD
515 lacks fine mode dust, the retrieved D_{eff} can still provide almost identical dust optical properties in TIR as the AER-D
PSD has based on the constraint from the retrieved $\text{DAOD}_{10\mu\text{m}}$. In other words, the combination of $\text{DAOD}_{10\mu\text{m}}$ and
 D_{eff} with comparable accuracy as in-situ measurements but better spatiotemporal coverage is a valuable tool for
reducing the global mean LW dust DRE uncertainties due to DAOD and dust particle size.

On the other side, all three optical properties calculated based on the AERONET PSD are bias low compared with
520 that based on AER-D and the retrieved PSD. As the fine-mode PSD has a negligible impact on dust optical properties
in TIR, the result suggests that the AERONET coarse-mode PSD is highly likely to be underestimated in terms of
size, which has been pointed out in several studies comparing AERONET PSD with other in-situ measurements
(Müller et al., 2010; Müller et al., 2012; McConnell et al., 2008; Adebisi et al., 2023). Due to the difficulties of
comparing the PSD from the column-integrated retrieval to that from the lofted-layer measurement (Toledano et al.,
525 2019), the possible reasons are as-of-yet not well-explained, which require detail investigations in the future.

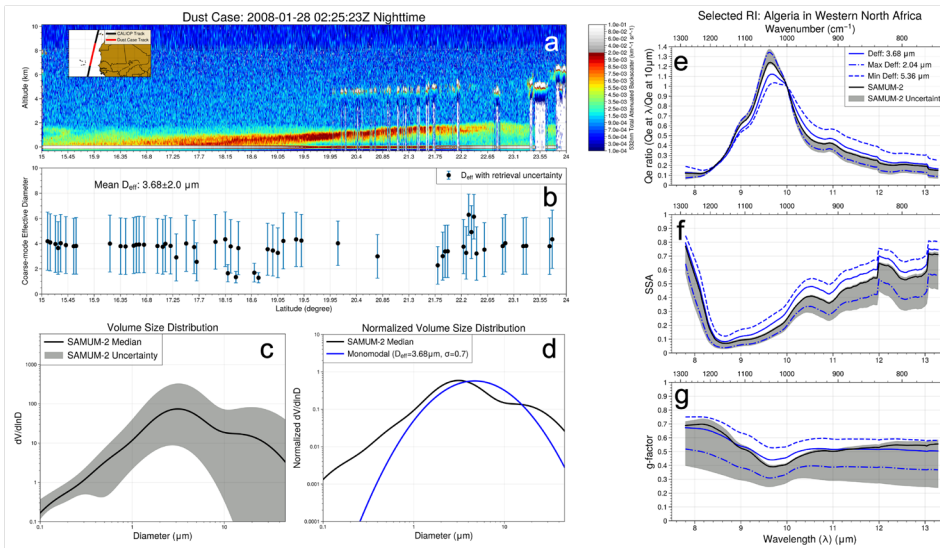
4.2 Evaluation of D_{eff} with SAMUM-2 and SALTRACE in-situ measurements

Noting that limiting the validation of D_{eff} with one case may be biased. To better demonstrate the reliability of the D_{eff}
retrieval, we compare the retrieved D_{eff} with in-situ measured dust PSDs from two additional field campaigns. One is
from the second field experiment of the Saharan Mineral Dust Experiment project (SAMUM-2) in the Cape Verde
530 area during January to February 2008 (Weinzierl et al., 2011). The other is the Saharan Aerosol Long-Range Transport
and Aerosol–Cloud–Interaction Experiment (SALTRACE) that is taken place over the North Africa, the Atlantic
Ocean, and the Caribbean from June to July 2013 (Weinzierl et al., 2016).

4.2.1 Comparison of D_{eff} with SAMUM-2 – A case over Cape Verde in winter

To compare with the SAMUM-2 campaign, we perform the retrieval for a nighttime dust case observed eastward Cape
535 Verde on Jan 28, 2008, as shown in Figure 6. Figure 6a shows the dust case is a low-altitude-level case up to $\sim 2 \text{ km}$,
consistent with the dust sampling of the experimental flights on January 28th in SAMUM-2 (see Table 2 and Figure 9
in Weinzierl et al. (2011)). As shown in Figure 6b, the mean retrieved D_{eff} is $3.68 \mu\text{m}$, which is further used to construct
the corresponding PSD for the comparison with SAMUM-2 dust PSD (see Figure 6c). In this case, we implement the
retrieval using the RI assignments introduced in Section 3.1.2 and Appendix C instead of performing HYSPLIT back

540 trajectories to identify dust source regions. In addition, this wintertime dust case has lower dust loading (not shown) than the summertime case in Section 4.1, leading to a lower information content for retrieving D_{eff} (see Figure 2a). Therefore, there is a mean retrieval uncertainty of $2.0 \mu\text{m}$ larger than the summertime case.



545 **Figure 6: (a) The CALIOP total attenuated backscatter at 532 nm on January 28th, 2008, over the downwind region of the Sahara Desert (the orbit at upper left). (b) The retrieved D_{eff} (black dots) of the cloud-free dust-laden profiles with the retrieval uncertainty (cyan error bars). (c) The volume lognormal ($dV/d\ln D$) SAMUM-2 PSD (black) with gray shadow area indicating the range of the measurement value from 3- to 97- percentile obtained from Weinzierl et al. (2011). (d) The normalized $dV/d\ln D$ of SAMUM-2 (black) and the retrieved coarse mode PSD corresponding to $D_{\text{eff}} = 3.68 \mu\text{m}$ (blue). (e-g) The Q_e ratio to $10 \mu\text{m}$ (e), SSA (f), g-factor (g) calculated based on the SAMUM-2 PSD (black) with its uncertainty (grey area) and the retrieved coarse mode PSD (blue) with the retrieval uncertainty (blue dash curve for the lower bound; blue dash-dot curve for upper bound).**

550

In Figure 6d, we found that the monomodal PSD corresponding to the mean retrieved D_{eff} agrees with SAMUM-2 PSD by having the peak between the third and fourth modes of SAMUM-2 PSD. Due to the limitation of the fixed assumption of the lognormal volume distribution's standard deviation, the monomodal PSD overestimates dust with D_p from 4 to $13 \mu\text{m}$ but underestimates dust with $D_p > 13 \mu\text{m}$. Because of that, the Q_e ratio, SSA and g-factor corresponding to the monomodal PSD have slight differences from that of the SAMUM-2 PSD in the TIR spectral region. However, the dust TIR optical properties of the two PSDs are generally consistent after considering their uncertainties. It shows the D_{eff} retrieval's capability to capture the seasonal differences of dust size in the Cape Verde area revealed by the AER-D and SAMUM-2 filed campaigns.

560

4.2.2 Comparison of D_{eff} with SALTRACE – A dust case transport throughout North Atlantic from June 12th to June 23rd, 2013

In order to evaluate the D_{eff} retrieval at long-range transport regions and demonstrate the variation of D_{eff} during the transport, we compare our results with the dust D_{eff} measured during the SALTRACE field experiment that studied a Lagrangian dust plume over both Cape Verde (SALTRACE-E) and Barbados (SALTRACE-W) on June 17th and June 22nd, 2013.

First of all, we perform the retrieval on a series of MODIS-CALIOP observations from June 16th within the Cape Verde area to June 23rd over the Caribbean Sea, as shown in Figure 7. In Figure 7a, the dust plume was vertically distributed between 2 km to 6 km, with the mean retrieved D_{eff} at 4.8 μm (Figure 7a2) on June 16th. From June 18th to 20th, the dust plume was transported to the mid-Atlantic ($\sim 43^\circ\text{W}$) and decreased the layer height from 2-5 km to 2-4 km (Figures 7b1 and 9c1). Meanwhile, the mean retrieved D_{eff} reduced from 4.3 μm to 4.0 μm (Figures 7b2 and 7c2). Figures 7d1 to 7f1 show that the dust plume traveled toward the Caribbean Sea from June 21st to June 23rd, maintaining the layer height between 1.5 km and 3.5 km and the retrieved D_{eff} at $\sim 3.9 \mu\text{m}$ (Figures 7d2 to 7f2). During the transport, the dust loading is also decreasing (see Figures 7a1 to 7f1), leading to lower information content for retrieving D_{eff} (see Figure 2a) and, therefore, relatively higher retrieval uncertainty (error bars in Figures 7a2 to 7f2).

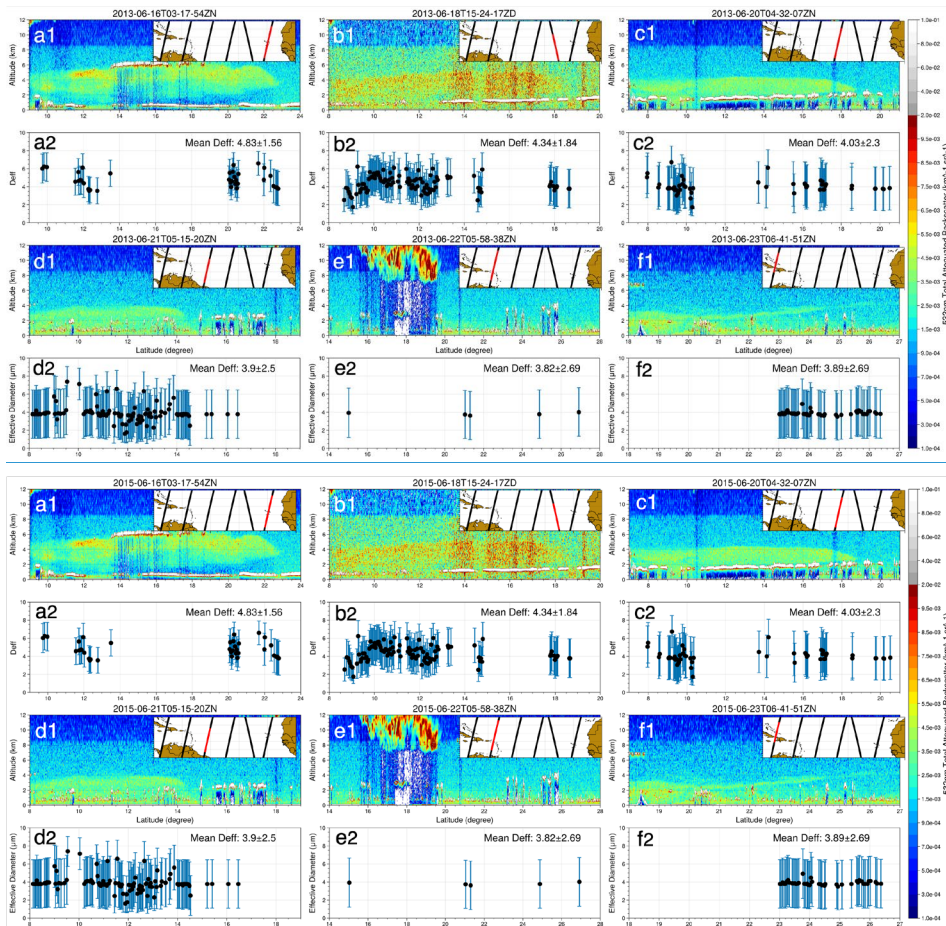


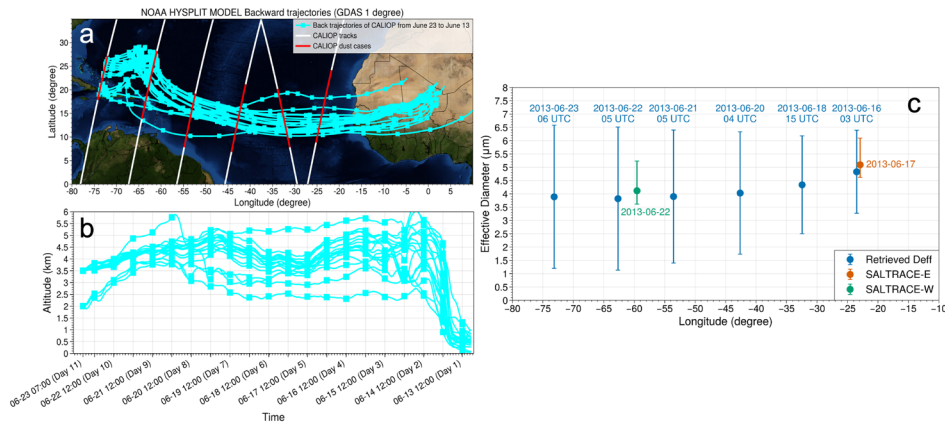
Figure 7: (a1 to f1) The CALIOP total attenuated backscatter at 532 nm on June 16th (a1), 18th (b1), 20th (c1), 21st (d1), 22nd (e1), 23rd (f1), 2013 (the orbit at upper left). (a2 to f2) The retrieved D_{eff} (black dots) of the cloud-free dust-laden profiles with the retrieval uncertainty (cyan error bars) corresponding to a1 to f1.

580

To prove that the MODIS-CALIOP observations snapshotted the transport processes of the same dust case that SALTRACE observes, we present the HYSPLIT back trajectories started from the MODIS-CALIOP observation on June 23rd over the Caribbean Sea, as shown in Figure 8. We set the dust layer heights at 2 km and 3.5 km at the starting point (see Figure 8b) to serve as the vertical boundaries of the observed dust plume on June 23rd (Figure 7f1). Figure 8a shows that the dust event originated from the North African source regions identified during SALTRACE (see Figure 5 in Weinzierl et al. (2016)) before June 13th. In addition, the dust case has transport trajectories overlapping with the MODIS-CALIOP observed dust plumes presented in Figure 7. Comparing Figure 8b with Figures 7a1 to 7f1,

585

590 we found that the vertical height of the dust plume varies between 2 km and 6 km during transport, which agrees with
the vertical dust distribution observed by MODIS-CALIOP. Therefore, we conclude that the MODIS-CALIOP dust
cases observe the same dust case as SALTRACE. However, we notice that the MODIS-CALIOP observational times
are not perfectly consistent with the back trajectory times, implying that the retrievals presented in Figure 7 may not
be the properties of the same air mass in the dust event as observed by SALTRACE. Thus, we do not expect a perfect
595 agreement between our retrieved D_{eff} and the SALTRACE measurements.



600 **Figure 8: The distribution of the spatial (a) and the vertical (b) ensemble HYSPLIT back trajectories on the CALIOP dust case from 2013-06-23 back to 2013-06-12 (cyan rectangle solid lines). The white solid curves represent the MODIS-CALIOP orbit tracks that observed the dust cases presented in Figure 7, which are highlighted in red curves. (c) The D_{eff} versus the longitudes of the MODIS-CALIOP retrievals in Figure 7 (blue dots), the SALTRACE-E at Cape Verde (red dot) and the SALTRACE-W at Barbados (green dot). The corresponding error bars represent their retrieval uncertainties and in-situ measured uncertainties.**

605 Figure 8c shows the retrieved mean D_{eff} of the MODIS-CALIOP observed dust plumes in Figure 7 and the D_{eff} of SALTRACE-E at Cape Verde and SALTRACE-W at Barbados. The retrieved D_{eff} on June 16th over Cape Verde (4.8 μm) is close to that of SALTRACE-E (5.1 μm). During the transport from Cape Verde (23°W) to mid-Atlantic (43°W), the D_{eff} decreases from 4.8 μm to 4.0 μm . Approaching Barbados and further the Caribbean Sea, the D_{eff} remains at 3.9 μm , which is also close to that of SALTRACE-W (4.1 μm). It validates the D_{eff} retrieval in both the short-range and long-range transport regions and demonstrates the retrieval's capability of revealing the transport process of dust
610 coarse-mode particle size in a better spatiotemporal resolution than in-situ measurements.

5 Climatological analyses

5.1 Comparison of DAOD_{10μm} with IIR-based DAOD_{10.6μm} and IASI-based DAOD_{10μm}

In addition to the presented case studies, the statistical evaluation of satellite-based retrieval of DAOD usually assumes the AERONET AOD in VIS as the benchmark. However, the comparison between DAOD_{10μm} and AERONET AOD necessitates the conversion of DAOD from TIR to VIS, which introduces additional uncertainties stemming from the assumed thermal-to-visible DAOD ratios. Moreover, in our case, a pixel-by-pixel comparison with AERONET poses challenges as CALIOP has limited spatial coverage, thus providing inadequate AERONET-collocated samples.

Formatted: Subscript

Therefore, in this section, we statistically evaluate the MODIS-CALIOP DAOD_{10μm} by comparing it with the three independent TIR-based satellite-retrieved DAOD_{TIR} datasets that are rigorously assessed through comparisons with AERONET COD_{500nm}. The first one is the night-time-only IIR-based DAOD_{10.6μm} from Z22. Note that the IIR-based retrieval has two DAOD_{10.6μm} datasets based on two different dust PSD assumptions. We use the one based on the Fennec SAL PSD from Ryder et al. (2013a) (referred to as “Fennec-SAL DAOD_{10.6μm}”) recommended from Z22. The second one is the IASI-based dataset, as mentioned in Section 1. It retrieves DAOD_{10μm} and dust mean layer altitude based on a two-step LUT method developed by the research group at Laboratoire de Météorologie Dynamique (LMD) (referred to as “IASI-LMD”). The third one retrieves DAOD_{10μm} using IASI based on an artificial neural network (NN) method developed by the research group at Université libre de Bruxelles (ULB) (referred to as “IASI-ULB”) (Clarisse et al., 2019).

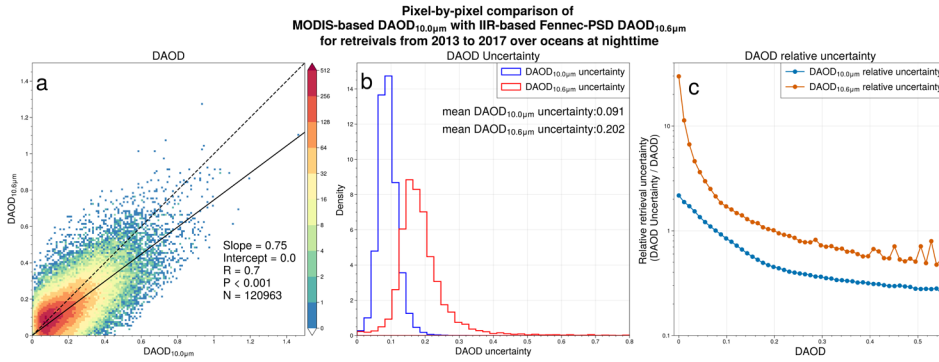
As the IIR Fennec-SAL DAOD_{10.6μm} can be easily collocated with the MODIS-CALIOP DAOD_{10μm}, we perform a pixel-by-pixel comparison between the two datasets using the five-year retrievals from 2013 to 2017 at nighttime based on a two-step collocation method. As mentioned in Z22, the IIR-based retrieval is implemented on samples with the estimated DAOD_{532nm} > 0.05, while the MODIS-CALIOP retrieval does not carry this limitation. Consequently, we first choose the MODIS-CALIOP DAOD_{10μm} with the corresponding estimated DAOD_{532nm} > 0.05 in both products. Note that the MODIS-CALIOP DAOD_{10μm} is retrieved simultaneously with D_{eff} while the IIR Fennec-SAL DAOD_{10.6μm} was retrieved with a fixed D_{eff} ~ 6.7 μm. Therefore, to control the dust PSD impact on the retrieved DAOD, we further select the MODIS-CALIOP DAOD_{10μm} with D_{eff} ranging from 4 μm to 8 μm to collocate with the Fennec DAOD_{10.6μm}.

As shown in Figure 9a, the DAOD_{10μm} correlates with DAOD_{10.6μm} with R = 0.7 and with DAOD_{10.6μm} being systematically lower than DAOD_{10μm} by 25% (slope = 0.75). The difference may be attributed to the spectral difference between 10.0 μm and 10.6 μm (see Figure 5c), which ranges from 0.5 to 0.8 for D_{eff} ranging from 4 μm to 8 μm. In addition to spectral differences, several factors may have caused the variability of the collocated pixels between the two datasets. Firstly, although the collocated DAOD_{10μm} are pre-selected based on D_{eff}. The impact of dust PSD on the retrieved DAOD still exists, as it is challenging to find enough pixels with the same D_{eff} as the Fennec SAL observation. Secondly, the treatments of RI in the two studies are also different. In Z22 a relatively simple method is used to assign the Di-Biagio RI to different regions while we utilize the DustCOMM-2021 to help assign Di-Biagio

650 RI in this study (see Appendix C). Furthermore, the MODIS-CALIOP retrieval has evolved from the IIR-based retrieval from Z22 with three improvements, namely the lower detector noise from MODIS, the improved retrieval methods, and the enhanced dust RI assumptions. These differences may have also directly affected the pixel-by-pixel comparison.

Thanks to the abovementioned improvements, in Figure 9b, the histogram of the absolute DAOD uncertainty of DAOD_{10μm} is reduced by ~55% from 0.2 to 0.09 in terms of the mean value compared with that of DAOD_{10.6μm}. In Figure 9c, the relative uncertainty of DAOD_{10μm} is substantially reduced compared with that of DAOD_{10.6μm}, especially for retrievals with small DAOD value (e.g., DAOD_{10μm} < 0.1). Consequently, we conclude that the MODIS-CALIOP DAOD_{10μm} is generally consistent with the IIR-based DAOD_{10.6μm} from Z22 with a substantial improvement regarding the retrieval uncertainty

660



665 **Figure 9: The pixel-by-pixel comparison of MODIS-CALIOP DAOD_{10μm} with the IIR-based Fennec-SAL DAOD_{10.6μm} from Z22 for retrievals from 2013 to 2017 over oceans at nighttime. (a) The joint histogram of DAOD_{10μm} and DAOD_{10.6μm}. The solid black line is the linear regression of the two datasets. The R, P and N at the lower right represent the Pearson correlation coefficient, p-value and the number of pixels of the linear regression. (b) The probability density function (PDF) of DAOD_{10μm} uncertainty (blue) and DAOD_{10.6μm} uncertainty (red). (c) The mean relative retrieval uncertainty (i.e., DAOD uncertainty / DAOD) of DAOD_{10μm} (blue) and DAOD_{10.6μm} (red). The y-axis is on a logarithmic scale.**

670

Unlike the comparison with the IIR-based retrieval, the orbit difference between the MODIS-CALIOP and IASI observations and the cloud-free dust sampling difference between the corresponding retrievals prevent the pixel-by-pixel comparison with the Level-2 data (Zheng et al., 2022). Therefore, we alternatively perform the climatological comparison among the aggregated 5° longitude by 2° latitude Level-3 seasonal mean MODIS-CALIOP, IASI-LMD and IASI-ULB DAOD_{10μm} based on five-year data from 2013 to 2017 in both daytime and nighttime. The 5° by 2° seasonal mean IASI-LMD and IASI-ULB DAOD_{10μm} are aggregated from the corresponding 1° by 1° monthly mean

675

Level-3 products. Note that both seasonal mean IASI DAODs are divided by the total number of AOD samples. To be consistent, in our retrieval, the seasonal mean $DAOD_{10\mu m}$ is averaged by the total number of cloud-free aerosol samples ($N_{aerosol}$ in Figure S109).

Figure 10 shows the seasonal mean $DAOD_{10\mu m}$ over oceans in both daytime and nighttime averaged by five-year retrievals of MODIS-CALIOP (left column), IASI-ULB (middle column) and IASI-LMD (right column) from 2013 to 2017. Similar to Z22, we highlight three dust-transport regions, North Atlantic (NA), Indian Ocean (IO) and North Pacific (NP) and define the rest of the areas as non-dust-dominated regions as shown in Figure 10.

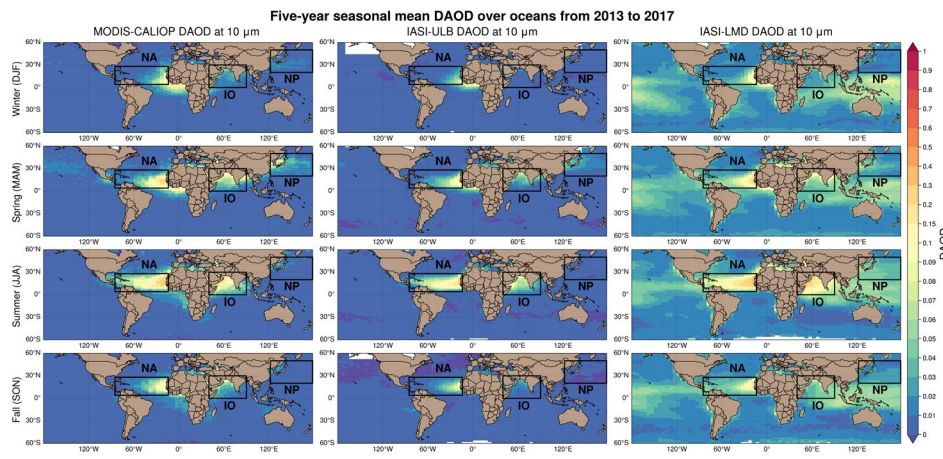


Figure 10: The five-year seasonal mean $DAOD_{10\mu m}$ comparison between the retrieval of MODIS-CALIOP (left column), the IASI-ULB and the IASI-LMD. From the top row to the bottom presents seasons from winter to fall. The black boxes indicate the three defined dust-transport regions, North Atlantic (NA; 4°N-30°N, 90°W-14°W), Indian Ocean (IO; 0°N-30°N, 40°E-90°E) and North Pacific (NP; 20°N-50°N, 120°E-180°).

In terms of seasonal variation, the MODIS-CALIOP retrieval well captures the seasonal patterns of $DAOD$ over the three dust-transport regions compared with IASI-ULB and IASI-LMD. Over non-dust-dominated regions, the MODIS-CALIOP $DAOD_{10\mu m}$ agrees more with IASI-ULB, while IASI-LMD $DAOD_{10\mu m}$ is bias high (~ 0.05). In boreal winter, $DAOD_{10\mu m}$ over tropical and southern Atlantic reach the peak, indicating that dust emitted from North Africa is transported south-westward and reaches south America due to the south-shifted Harmattan north-easterly wind (Marticorena et al., 2010). Dust transport westward over NP originates from east Asian source regions, such as the Gobi Desert and Taklimakan Desert, with peak emission in the spring (Yu et al., 2010). Therefore, $DAOD_{10\mu m}$ over NP is found at its peak in spring, mainly driven by mid-latitude westerly jets with relatively high altitudes (> 5 km). Because of the higher altitude of Asian dust compared with North African dust, it also has a longer transport distance to reach NP and even to North America (Huang et al., 2022), but with relatively lower $DAOD_{10\mu m}$ (0.05-

705

0.1 compared with that over NA (~0.2). From spring to summer, dust from North Africa outbreaks in both NA and the Mediterranean Sea and peaks in summer. With the peak emission in North Africa in summer, dust transport to NA has the highest DAOD10 μ m (> 0.3) and reaches North America with relatively high DAOD10 μ m (~0.1) compared with other seasons. In addition, DAOD10 μ m over IO peaks in summer (~0.2), mainly due to the summer Shamal wind bringing dust from Arabian Peninsula and traveling southwestward to IO. Both DAOD10 μ m over NA and IO decrease from summer to autumn due to the reduced emission from both source regions.

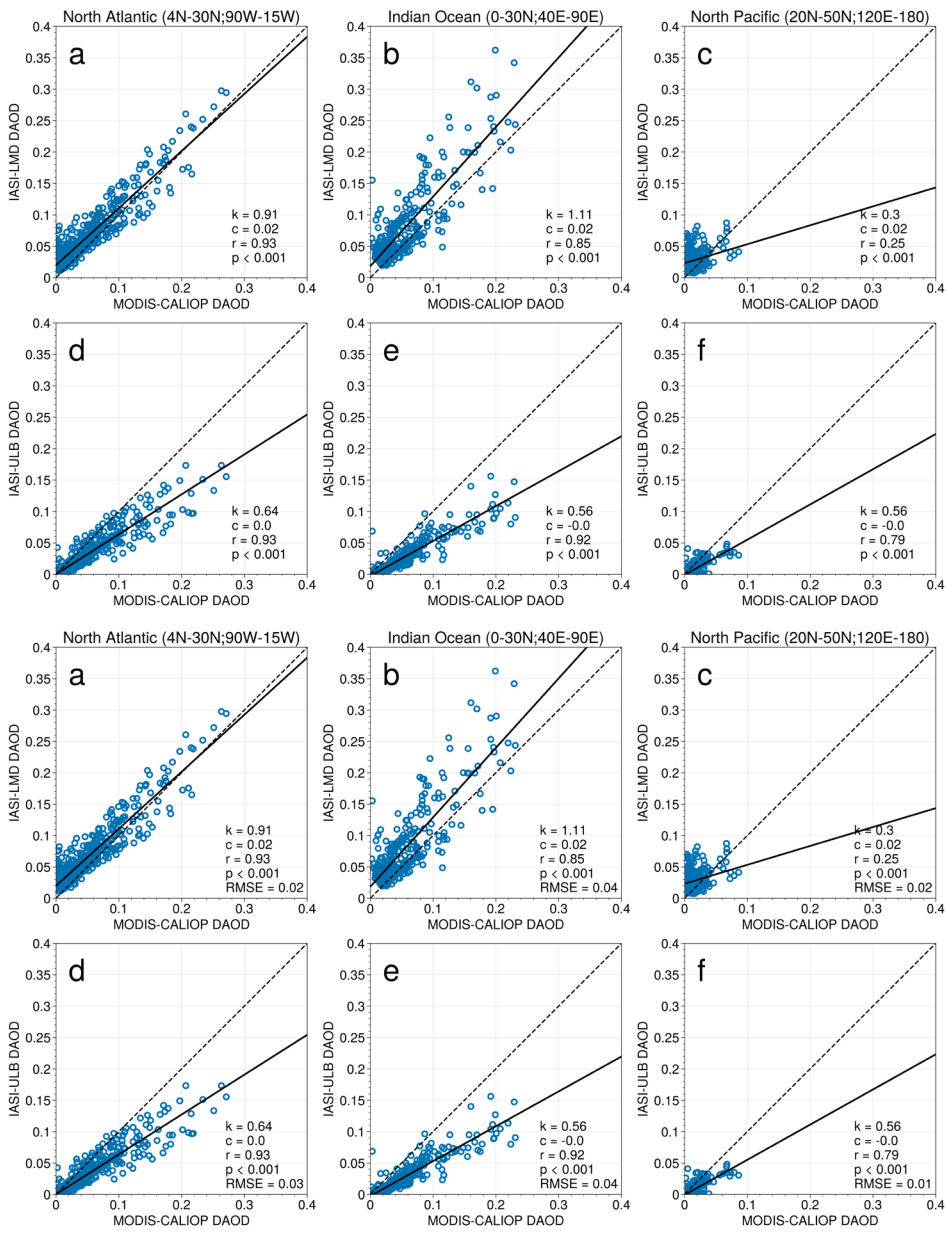


Figure 4011: The comparisons of the seasonal mean MODIS-CALIOP DAOD_{10µm} versus IASI-LMD (a,b,c) and IASI-ULB (d,e,f) DAOD_{10µm} over NA (a,d), IO (b,e) and NP (c,f) from 2013 to 2017. Each point in the scatterplots represents a seasonal

715 mean DAOD_{10μm} in one of the 5° by 2° grids for a specific year from 2013 to 2017. The solid black lines are the linear regressions of each comparison, while the black dash lines are the reference one-to-one lines. The k, c, r, and p and RMSE at the upper right of each panel represent each linear regression's slope, intercept, correlation coefficient, and p-value and root mean square error.

720 For more quantitatively comparison, Figure 11 shows the 2-D histogram of all the Figure 10 shows the comparisons of 5° by 2° gridded seasonal mean samples in each year from 2013 to 2017 of MODIS-CALIOP DAOD_{10μm} with the two IASI DAOD_{10μm} over the three dust-transport regions from 2013 to 2017. MODIS-CALIOP DAOD_{10μm} over NA and IO are highly correlated and consistent with IASI-LMD DAOD_{10μm} with R = 0.9, 0.8 and k = 0.9, 1.1, respectively, as shown in Figures 10a-11a and 10b-11b. However, for optically thin dust (e.g., DAOD < 0.1), IASI-LMD DAOD_{10μm} is systematically ~0.02 greater than MODIS-CALIOP DAOD_{10μm} as shown from the intercepts of the linear regression in Figures 10a-11a and 10b-11b. In addition, the two datasets have a poor agreement over NP (R = 0.2). In contrast, 725 MODIS-CALIOP DAOD_{10μm} achieves a better correlation over the dust-transport regions with IASI-ULB (including NP) than the comparison with IASI-LMD DAOD_{10μm} (see Figures 10d-11d-10f-11f). It is mainly because both retrievals mostly avoid contamination from sub-pixel clouds and background aerosols, which should be the reason for the high bias of the IASI-LMD optically thin dust (DAOD_{10μm} < 0.1) DAOD_{10μm}. However, IASI-ULB DAOD_{10μm} is 40%-60% lower than that of MODIS-CALIOP and IASI-LMD DAOD_{10μm} over the three dust-transport regions (k = 0.6, 0.5, 0.4 730 in Figures 10d-11d-10f-11f).

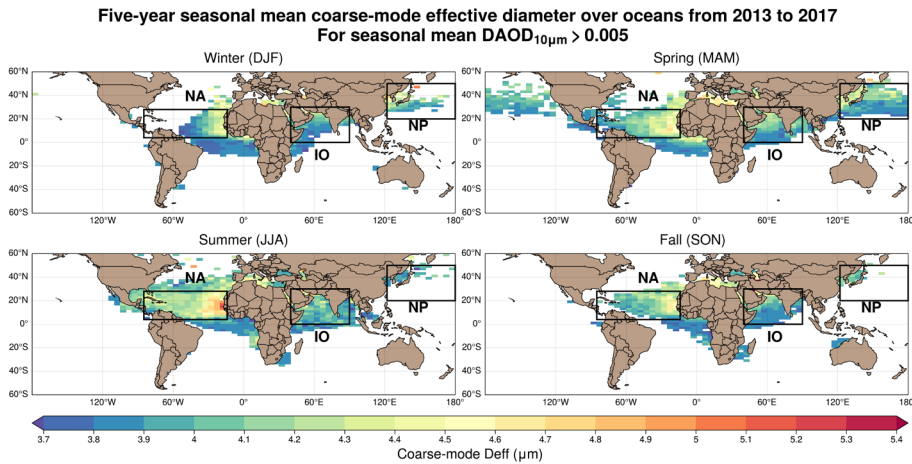
Although the discrepancy of the two IASI-based DAOD_{10μm} is non-negligible, the two datasets achieve good agreements with AERONET because the different assumptions of TIR-to-VIS DAOD ratios offset the DAOD_{10μm} difference. As they assumed similar dust RIs (e.g., OPAC RIs) and spherical dust, the disagreement of the DAOD_{10μm} 735 could be due to the different *a priori* dust PSDs. IASI-ULB assumes a monomodal dust PSD with a geometric mean radius at 0.5 μm (i.e., mean diameter at 1.0 μm). It is much smaller than the IASI-LMD assumed coarse-mode dust PSD with an effective radius at 2.3 μm (i.e., effective diameter = 4.6 μm), possibly leading to the systematically lower DAOD_{10μm} compared with MODIS-CALIOP and IASI-LMD DAOD_{10μm}. Because MODIS-CALIOP D_{eff} has a climatological value ranging from 4.0 to 5.0 (see Figure 11-12, detail in Section 5.2), which is closer to 4.6 μm, 740 MODIS-CALIOP DAOD_{10μm} shows better consistent with the IASI-LMD DAOD_{10μm}. This non-negligible dependency of the retrieved DAOD_{10μm} to dust PSD is also presented in Z22. It highlights the importance of the spatiotemporal variation of dust PSD and the advantage of the observational constraint on both DAOD_{10μm} and dust coarse-mode PSD from the MODIS-CALIOP retrieval.

745 5.2 Spatiotemporal variation of dust D_{eff}

One of the main objectives of this study is to provide a climatological view of dust coarse-mode size variation during transport in a global coverage from satellite observations, which has not yet been available in the literature, as far as we know, due to the difficulties mentioned in Section 1. In this section, we present the spatiotemporal variation of D_{eff}

750 in terms of seasonal variation, the regional difference among dust-transport regions and longitudinal-mean variation within dust-transport regions based on the five-year retrieval data from 2013 to 2017.

755 Different with seasonal mean $DAOD_{10\mu m}$, the denominator of the seasonal mean D_{eff} is the number of samples with successful retrievals only. Noting that the retrieval uncertainty is large for optically thin dust (i.e., $DAOD_{10\mu m} < 0.1$, see Figure 9c), we consider that the seasonal mean $DAOD_{10\mu m} < 0.005$ is mainly contributed by optically thin dust and therefore mask the seasonal mean D_{eff} with seasonal mean $DAOD_{10\mu m} < 0.005$ to focus on more confident D_{eff} retrievals. We found that the seasonal variation of D_{eff} is highly correlated with that of $DAOD_{10\mu m}$. For example, the largest D_{eff} over NA and IO occurs in summer, while the peak of D_{eff} over NP happens in spring. As dust extinction in TIR is more sensitive to coarse-mode dust (Ryder et al., 2019), it is reasonable to find that the greater the $DAOD_{10\mu m}$, the coarser dust is in the atmosphere.



760 **Figure 4412:** 2013-2017 five-year averaged seasonal mean D_{eff} masked by the five-year seasonal mean $DAOD_{10\mu m} > 0.005$ in winter (a), spring (b), summer (c) and fall (d). The black boxes indicate the three defined dust-transport regions as same as in Figure 9.

765 In terms of regional differences, we found that the maximal seasonal D_{eff} over IO ($\sim 4.2 \mu m$ in summer, Figure 4412c) and NP ($\sim 4.2 \mu m$ in spring, Figure 4412b) are $\sim 22\%$ lower than that over NA ($\sim 5.4 \mu m$ in summer, Figure 4412c). It suggests that the coarse-mode dust is frequently found over NA but not over IO and NP. It is expected over NP because the transport distance from source regions located in East Asia to NP is much longer than that from North Africa to NA (Alizadeh-Choobari et al., 2014). In addition, the emitted and transported dust PSD from Asia is possible to be finer than that from North Africa and Arabia due to the radiative feedback on dust emission (Woodage and Woodward, 2014). As a result, there is less chance for coarse dust particles to survive till over NP. In contrast, although dust from the Middle East to IO has a similar transport distance as that over NA, fewer coarse dust particles are found

770

over IO. As the retrieval samples are distributed similarly over the three transport regions for all seasons as shown in Figure S109, it is less likely to have sampling bias between regions. One of the possible reasons that the long-range transport dust from the Middle East is not within elevated mixed layers (Carlson, 2016), such as SAL over NA, that triggers static instability and strong vertical turbulence to sustain coarse dust particles for a longer lifetime (Gutleben and Groß, 2021; Gasteiger et al., 2017). However, due to insufficient in-situ measurements on dust PSD in the Middle East (Adebiyi et al., 2020b), what causes the regional differences in dust particle size after long-range transport remains open and needs further investigation in the future.

775

780

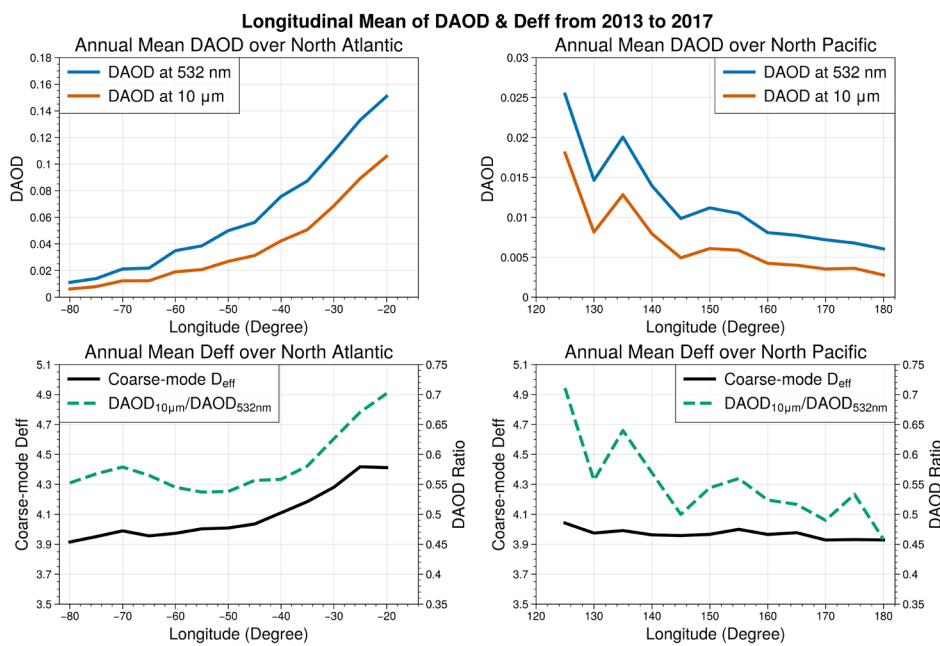


Figure 4213: The annual longitudinal mean $DAOD_{10\mu m}$ (blue curves), $DAOD_{532nm}$ (red curves), the DAOD ratio of $DAOD_{10\mu m}$ to $DAOD_{532nm}$ (green dash curves) and D_{eff} (black curves) over the North Atlantic (a,c) and the North Pacific (b,d).

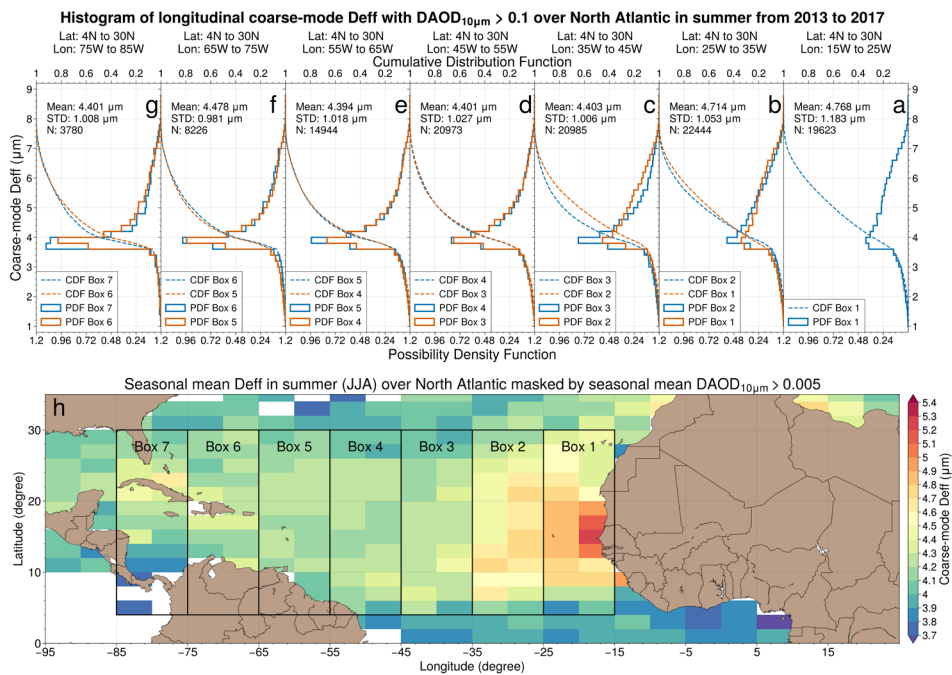
785

As mentioned in Section 5.1, the assumed dust PSD impacts heavily on both the retrieved $DAOD_{10\mu m}$ and the theoretical TIR-to-VIS DAOD ratio. Because our retrieval provides simultaneous $DAOD_{10\mu m}$ and D_{eff} and the synergistic CALIOP estimated $DAOD_{532nm}$, we further investigate the relationship between D_{eff} and the observational-based TIR-to-VIS DAOD ratio (defined as $DAOD_{10\mu m}/DAOD_{532nm}$). From the view of longitudinal transport for Saharan dust and Asian dust, we demonstrate the annual longitudinal mean $DAOD_{532nm}$ and $DAOD_{10\mu m}$ over NA and NP (Figures 42a-13a and 42b-13b). They both show a consistent variation between $DAOD_{532nm}$ and $DAOD_{10\mu m}$ with a decreasing trend westward over NA and eastward over NP, convincing the reliability of the $DAOD_{10\mu m}$ retrievals

790

described in Section 5.1. Figures [42e-13c](#) show that the corresponding DAOD ratio over NA decreases by 23% westward from 18°W to 40°W and 8% from 40°W to 80°W. As coarse-mode particles dominate the dust extinction in TIR, the reduction of the DAOD ratio reflects the faster decrease of $DAOD_{10\mu m}$ and, thus, implies a loss of coarse-mode dust loading in the column, which also can be inferred by the decreasing of D_{eff} . In Figure [42e13c](#), we found that the decreasing trends of D_{eff} and DAOD ratio are highly correlated. It demonstrates a ~20% reduction of DAOD ratio and a ~7% decrease of mean D_{eff} during the transport to the mid-Atlantic, while there are less than 10% and 2% decrease of DAOD ratio and mean D_{eff} during the rest of the NA transport. The transport pattern over NA is also similar with the dust case observed by SALTRACE presented in Section 4.2.2. However, in Figure [42d13d](#), we found a rapid fluctuation of the DAOD ratio due to the fewer retrieval samples (Figure [S109](#)) and higher retrieval uncertainty from 120°E to 140°E, which is against D_{eff} 's relatively stable decreasing rate. Despite that, we found a less than 10% reduction of D_{eff} throughout the eastward transport to 180°, suggesting a stable trend of dust coarse-mode size during the NP transport.

Note that dust particle size varies in the day-to-day transports, which is not visible in the long-term averaged longitudinal transport. To provide details on the variation of D_{eff} in different size ranges during transport over NA and NP in their peak season, we present the population distribution of D_{eff} longitudinally in summer over NA and spring over NP. We first slice the NA region from 4°N to 30°N into seven sub-regions at 10° longitude intervals, as shown in Figure [43h14h](#). Within each sub-region box, we present the histogram and the cumulative distribution function (CDF) of D_{eff} of all the optically thick dust (i.e., $DAOD_{10\mu m} > 0.1$) in the summer from 2013 to 2017. To better visualize the variation of D_{eff} during the transport, within each sub-region box, the histogram and CDF (blue curves in Figures [43a-14a](#) to [43g14g](#)) are compared with those from the previous (i.e., eastward) box are also presented (red curves in Figures [43b-14b](#) to [43g14g](#)).



815

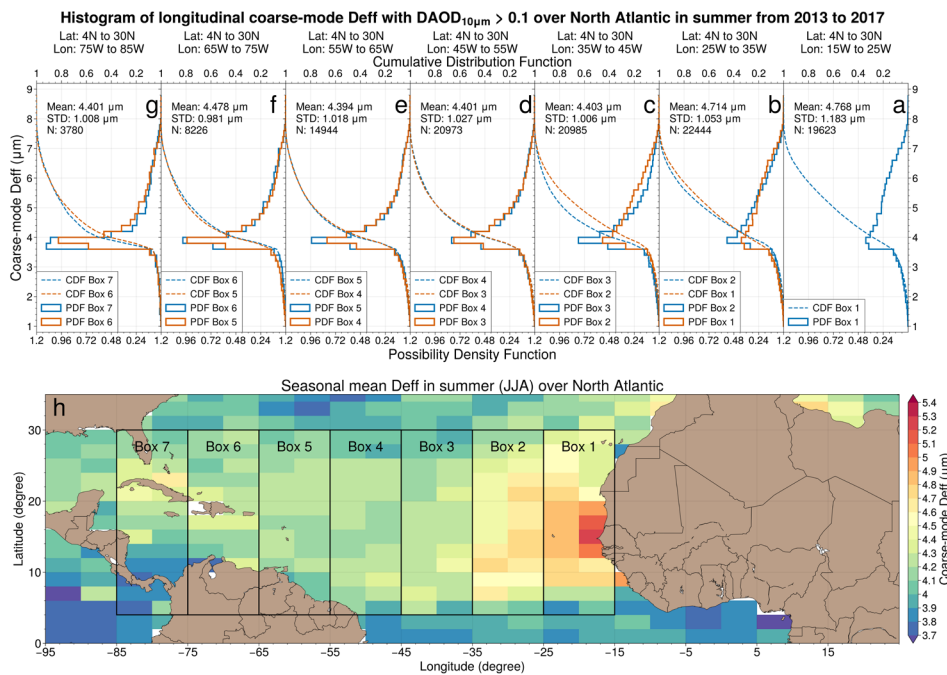
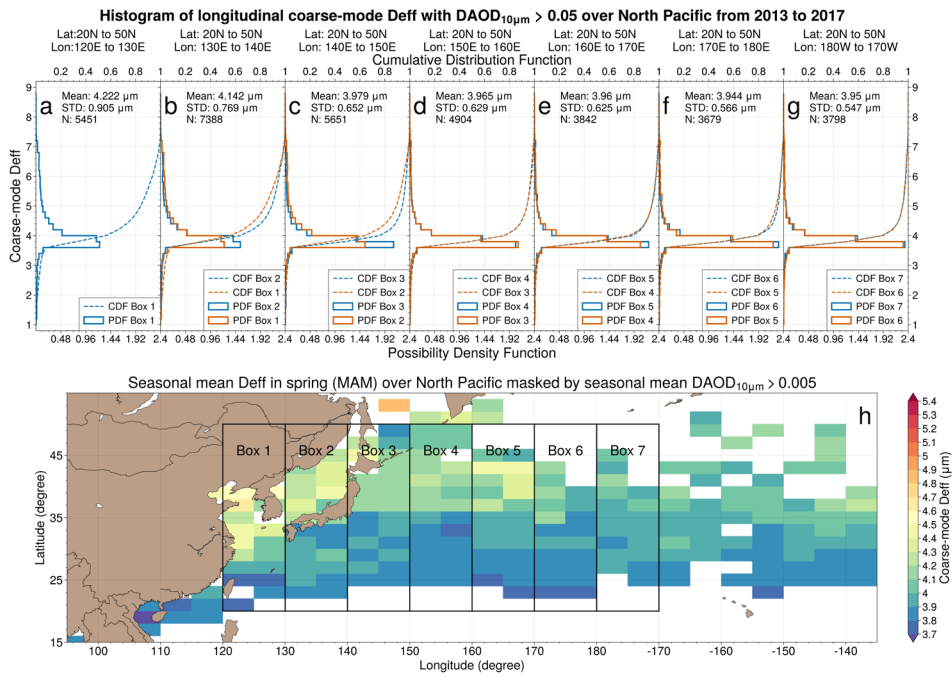


Figure 1314: The histogram (solid curves with the bottom x-axis) and the cumulative distribution function (dash curves with the top x-axis) of D_{eff} with $DAOD_{10\mu m} > 0.1$ within each longitudinal box from west to east ranging from 1 (a) to 7 (g) over the NA in the summer from 2013 to 2017. Blue curves represent D_{eff} samples within the current box. Orange curves represent D_{eff} samples within the previous box eastward. (h) The geolocation boundaries of each longitudinal box on top of the seasonal mean D_{eff} were masked by seasonal mean $DAOD_{10\mu m} > 0.005$ over the NA in the summer from 2013 to 2017.

Figures 13a-14a to 13b-14b show a slight decrease in the population of D_{eff} greater than $5.5 \mu m$. From Figures 13b-14b to 13e-14e, according to the CDFs, the contribution of $D_{eff} > 5 \mu m$ to the total number reduced from 40% to 20%. In PDFs, there is a ~50% reduction in the population of $D_{eff} > 5 \mu m$, while ~20% more dust with $D_{eff} \sim 4 \mu m$ is found, leading to the reduced mean D_{eff} from $4.7 \mu m$ to $4.4 \mu m$. Meanwhile, the peak of the PDFs in Figures 13a-14a to 13g-14g remains stable at $4.0 \mu m$, while the number of samples decreases gradually, as shown in PDFs in Figures 13d-14d to 13g-14g, indicating that less coarse-mode dust can be transported to Boxes 5 to 7 ($55^\circ W$ to $85^\circ W$).

The result suggests that ~50% of relatively coarser dust ($D_{eff} > 5 \mu m$) tends to drop out when transported to the mid-Atlantic ($25^\circ W$ to $35^\circ W$), which is ~2000 km away from source regions over North Africa. Afterward, from the mid-Atlantic to the Caribbean Sea, the mean D_{eff} remains almost unchanged, agreeing with the arguments from previous studies that the stabilization of coarse-mode dust PSD during the long-range transport (Weinzierl et al., 2017; Denjean et al., 2016; Ryder et al., 2019). Additionally, dust samples with $D_{eff} > 5 \mu m$ can still be found even at $65^\circ W$ and $75^\circ W$

835 (see Figures [13f14f](#) and [13g14g](#)) but with a relatively lower frequency (~20%). In other words, super-coarse dust particles, although rare, are still possible to be carried on a long-distance journey during the transport over NA (Van Der Does et al., 2018), which act against the gravitational settling theory by Stoke's law (Ginoux, 2003; Bagnold, 1974).



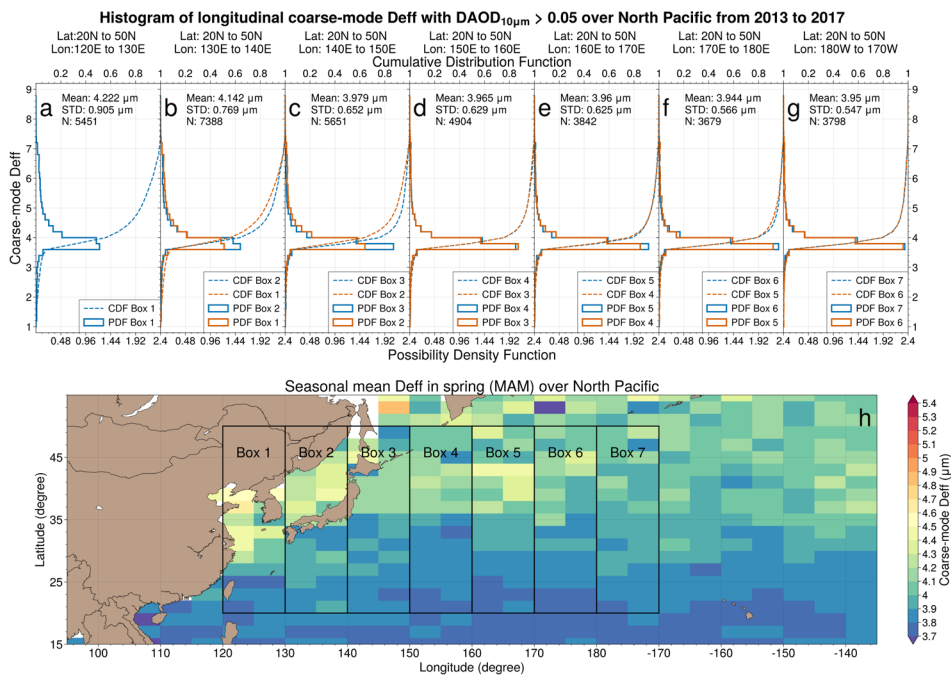


Figure 4415: Same as Figure 4314 but for D_{eff} with $DAOD_{10\mu\text{m}} > 0.1-05$ within each longitudinal box from west to east ranging from 1 (a) to 7 (g) over the NP in the spring from 2013 to 2017.

845 Unlike the Trans-Atlantic dust, Asian dust transport over NP experiences longer travel distances from the East Asian source regions and therefore has systematically smaller particle size. With the same method as Figure 4314, we present the histograms of D_{eff} with $DAOD_{10\mu\text{m}} > 0.05$ (according to the lower seasonal mean $DAOD_{10\mu\text{m}}$ over NP) within seven longitudinal boxes, as shown in Figure 4415. During the transport, the mostly unchanged PDFs with $D_{\text{eff}} > 4 \mu\text{m}$ from Box 1 (130°E) to Box 2 (140°E) only reduced ~10% from Box 2 to Box 3 (150°E). The CDFs are stable throughout the transport from Box 3 to Box 7 regardless of the total number of dust samples decrease. Compared with dust over 850 NA, only ~5% of dust with $D_{\text{eff}} > 5 \mu\text{m}$ can be found after transporting to Box 3. The relatively homogenous and stable distribution of $D_{\text{eff}} \sim 4 \mu\text{m}$ suggests that the coarse-mode dust particles over NP may also have longer lifetimes than expected by the stand-alone gravitational settling theory. However, as $DAOD_{10\mu\text{m}}$ and the number of successful retrievals over NP are lower than that over NA and IO, the relatively higher retrieval uncertainty prevents us from drawing a clear conclusion. Future studies are recommended to validate the satellite retrieved D_{eff} by in-situ measured 855 Asian dust PSDs.

6 Discussions and Conclusions

This study developed a novel retrieval algorithm for DAOD_{10 μ m} and the coarse-mode dust PSD represented by D_{eff} using the collocated CALIOP and MODIS observations. The D_{eff} retrieval is detailedly validated through three case studies in Aug 2015, Jan 2008 and June 2013, respectively.

We validate the DAOD_{532nm} matching with the AERONET total AOD at Cape Verde in the 2015 case study. Despite the spectral difference preventing the “apple-to-apple” comparison of DAOD_{10 μ m} with AERONET, the relatively good correlation between DAOD_{10 μ m} and the AERONET-validated DAOD_{532nm} demonstrate the DAOD_{10 μ m} retrieval’s reliability. Afterward, we present the consistency of the monomodal PSDs corresponding to the retrieved D_{eff} with the AER-D PSD and SAMUM-2 PSD as well as their TIR optical properties in the 2015 and 2008 cases. The 2013 case validates the D_{eff} retrieval in both the short-range (Cape Verde) and long-range (the Caribbean Sea) transport regions by comparing with SALTRACE dust PSD and demonstrates the retrieval’s capability of revealing the transport process of dust coarse-mode particle size in a better spatiotemporal resolution than in-situ measurements. The results convince us that the DAOD_{10 μ m} and D_{eff} retrieval dataset can provide a better constraint on regional and global LW DRE uncertainties due to DAOD and dust PSD. However, an assumption of dust RI is still needed.

We apply the retrieval to five-year MODIS-CALIOP data from 2013 to 2017 and compare the DAOD retrieval with IIR-based and IASI-based retrieval. As an improved version compared with the IIR-based retrieval, the MODIS-CALIOP retrieval reduced ~50% of DAOD uncertainty and achieves good consistency ($R = 0.7$ in Figure 9). In the climatological comparison with the seasonal mean IASI-based DAOD_{10 μ m}, MODIS-CALIOP DAOD_{10 μ m} reaches a better agreement with IASI-LMD DAOD_{10 μ m} over NA ($R = 0.9$) and IO ($R = 0.8$) than that over NP ($R = 0.2$). Meanwhile, the IASI-ULB DAOD_{10 μ m} over the three regions are highly correlated with MODIS-CALIOP DAOD_{10 μ m}, while they are systematically underestimated possibly due to the D_{eff} of the pre-assumed dust PSD is significantly lower than that of IASI-LMD DAOD_{10 μ m} and the climatological D_{eff}. The discrepancy of the two AERONET-evaluated IASI DAOD_{10 μ m} datasets reveals that the dependency of TIR-to-VIS DAOD ratios and the retrieved DAOD_{10 μ m} to dust PSD is non-negligible, which is also proved in Z22. It highlights the importance of considering the spatiotemporal variation of dust D_{eff} in TIR retrievals.

A global and climatological analysis of the five-year D_{eff} retrievals from -60°N to 60°N over oceans is presented. Comparing D_{eff} among the three transport regions, we found that seasonal mean D_{eff} over IO (3.9-4.2 μ m) is up to ~22% lower than that over NA (4.1-5.4 μ m) depending on different seasons, implying a shorter lifetime of coarse-mode dust particles transported from the Middle East to IO than that from North Africa to NA. For D_{eff} variation during transport, over NA, we found a ~50% reduction of retrievals with D_{eff} > 5 μ m from 15°W to 40°W and a relatively stable D_{eff} at ~ 4 μ m throughout the Caribbean Sea. The D_{eff} result from 15°W to 40°W differs from the IASI-retrieved effective radius distribution over NA in Peyridieu et al. (2013), which presented an almost constant value at 2 μ m during summer throughout the transport. In addition, the prevailing dust with D_{eff} at ~ 4 μ m and a small portion of dust with D_{eff} > 5 μ m (5%-20%) found after long-term transport in both NA and NP can hardly be explained

895 by the stand-alone gravity settling theory. The results provide observation-based transport patterns of the coarse mode dust size over oceans, which can be used to evaluate the simulated dust coarse mode PSD in dust transport models.

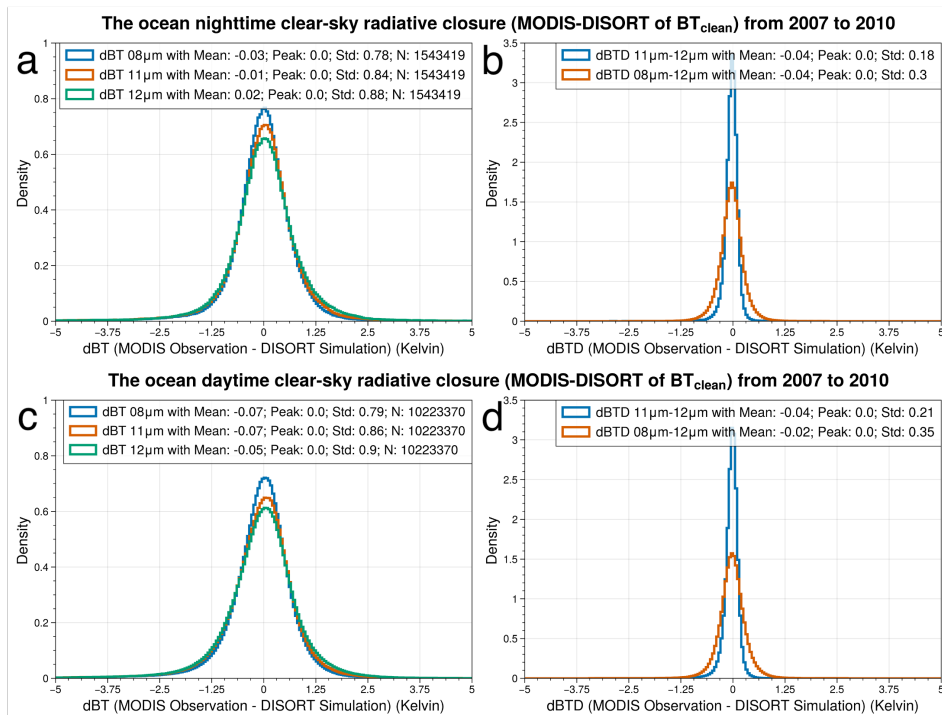
900 However, there are several limitations for our retrieval. First of all, the case-study validation of D_{eff} is limited to three field campaigns. Extended comparisons with ~~other~~ other-upcoming in-situ measurements, especially over Mediterranean, IO and NP, should be realized further to validate the applicability and significance of the proposed approach. Secondly, our retrieval is still not applicable for observations over land due to the uncertainties from land surface temperature and emissivity. Nonetheless, with more reliable databases of land surface characteristics, this portable retrieval algorithm can be easily extended to cover the dust source regions. Thirdly, the vertical distribution of dust PSD in columns is assumed to be homogeneous, which might be improved by inferring the layer attenuated backscatter total color ratio (i.e., the ratio of the layer total attenuated backscatter at 1064 nm to that at 532 nm) observed by spaceborne Lidars. ~~Thirdly~~ Lastly, the limited spatial coverage of CALIOP restrains the application of our data to regional studies. Extending the retrieval to off-CALIOP-track MODIS pixels is recommended for future studies.

910 **Appendix A: The cloud-free clean radiative closure benchmark between the CRTM-DISORT calculated and the MODIS-observed BTs**

In this study, the uncertainties contributed by the auxiliary data, the radiative transfer simulation, and the observational errors is evaluated through the radiative closure benchmark between the CRTM-DISORT calculated and the MODIS-observed BTs under cloud-free and clean (without dust) conditions based on the collocated MODIS and CALIOP data from 2007 to 2010.

Figures A1a and A1c show the BT discrepancies (referred to as “dBT”) between the simulations and the observations for daytime and nighttime cloud-free and clean cases over oceans at three MODIS TIR bands. Figures A1b and A1d show the corresponding discrepancies of the cloud-free spectral BT differences (BTD) between 11 μm and 12 μm (blue curve, referred to as “dBTD₁₁₋₁₂”) and that between 8.5 μm and 12 μm (red curve, referred to as “dBTD₀₈₋₁₂”). Both dBTs and dBTDs are unbiased (i.e., with a peak and a mean value centered at zero) in both daytime and nighttime, demonstrating a remarkable consistency between the CRTM-DISORT simulation and the MODIS observation. For the three single TIR BTs, because the 8.5- μm and 11- μm bands are the cleaner (i.e., less water vapor absorption) than the 12- μm band that is the most water-vapor-absorptive, the standard deviations of dBT at 8.5 μm and 11 μm are lower (0.78 – 0.86 K) than that at 12 μm (0.88 – 0.9 K). Interestingly, the errors of the two dBTDs are substantially reduced to the range of 0.2 to 0.4 K as the errors from the assumed atmospheric states at each band are canceled out, especially the dBTD₁₁₋₁₂ (0.18 K at nighttime and 0.21 K at daytime), which is sensitive to DAOD as explained in section 3.2. The smaller uncertainties in dBTDs are probably due to error cancellations. For example, if AMSR-E underestimates the SST, the simulated BT would be colder than the observation because of the overestimated surface-emitted radiance. However, the underestimation happens in all three TIR bands, and the error cancels each other to some extent, leading to smaller uncertainty in dBTDs.

Overall, one standard deviation of dBTs and dBTDs represents the retrieval uncertainty due to the atmospheric auxiliary data, the radiative transfer simulation, and the observational errors, which is revisited in section 3.2.



935 **Figure A1: The nighttime (a) and daytime (c) cloud-free and clean sky dBTs at the MODIS 8.5- μm (blue), 11- μm (orange) and 12- μm (green) bands. The nighttime (b) and daytime (d) cloud-free clean sky dBTD₈₋₁₂ (orange) and dBTD₁₁₋₁₂ (blue).**

940 **Appendix B: Pre-processing of the cloud-free dust detection from the collocated MODIS and CALIOP observation**

The first step of the retrieval is to identify high-quality cloud-free dust-laden observations. Due to the different spatial coverage of MODIS and CALIOP, the retrieval requires collocated data from both sensors, which is done in the following steps. First, we refer to the MODIS-AUX product (Partain, 2007) developed for CloudSat to find along-CloudSat-track MODIS pixels for two reasons. First, each along-CloudSat-track profile has 15 collocated MODIS pixels in the MODIS-AUX product. Each MODIS pixel contains the MODIS Level-1B radiances and Level-2 geometries. Using the 15 collocated MODIS pixels saves computational time from accessing the original terabyte-scale Level-1B products (Zheng et al., 2021). Second, the along-track orbits of CALIPSO and CloudSat are highly synchronized. It allows each along-CALIPSO-track profile to quickly match the nearest pixel among the 15 collocated along-CloudSat-track MODIS pixels. However, noting that the MODIS viewing zenith angle of the collocated pixels are not exactly nadir as CALIOP has, which is also considered in our retrieval (See Table 1).

945
950

The CALIOP “LID_L2_05kmAPro-Standard-V4” product has a 5 km along-track resolution, while the MODIS-AUX product is 1 km. To address this spatial difference, we reference the 1-km along-CALIOP-track geolocation records from the “IIR_L2_Track-Standard-V4” product, which provides five records with 1-km resolution in each 5-km CALIOP profile. Each of the five 1-km geolocation records is then used to find the nearest along-CloudSat-track MODIS pixels. The corresponding MODIS Level-1B 1-km TIR BTs, BT uncertainties and the MODIS sensor’s geometries (i.e., viewing/solar zenith/azimuth angles) are then assigned to each geolocation record.

Similar to the cloud masking process as in Z22, we use the collocated 1-km “Was_Cleared_Flag_1km” originated from the “IIR_L2_Track-Standard-V4” product to screen out MODIS pixels containing sub-pixel clouds that are detected by the single-laser-shot in 333 m along-track footprint. Finally, the remained cloud-free 1-km MODIS pixels within each 5-km CALIOP profile are averaged, forming the 5-km collocated MODIS-CALIOP cloud-free product.

After cloud masking, dust detection also follows the procedures described in Z22. Firstly, we identify the high-quality CALIOP backscatter profiles by applying the extinction control flag (“Extinction_QC_Flag_532 = 0, 1, 16, 18” (Winker et al., 2013; Yu et al., 2015a)) to the 5-km MODIS-CALIOP cloud-free product. Next, we apply the cloud-aerosol discrimination (CAD) score to select the profiles containing all detected features with CAD between -100 to -90 to ensure the quality of the detected aerosol layers (Yu et al., 2019). Finally, the selected CALIOP backscatter profiles are further used to distinguish dust from non-dust aerosols. The separation is based on the contrast of the DPR between dust and non-dust aerosols. The higher the non-sphericity and particle size, such as dust, the lower the DPR. Therefore, the DPR of dust aerosols (δ_d) is usually higher than that of other non-dust aerosols (δ_{nd}). Accordingly, a vertically resolved fraction $f_d(z)$ of dust backscatter ($\beta_d(z)$) to the observed backscatter ($\beta(z)$) (i.e., $f_d(z) = \beta_d(z)/\beta(z)$), is estimated by the observed particulate DPR $\delta(z)$, δ_d and δ_{nd} as

$$f_d(z) = \frac{(\delta(z) - \delta_{nd})(1 + \delta_d)}{(1 + \delta(z))(\delta_d - \delta_{nd})} \quad (\text{B1})$$

Following Yu et al. (2015a) and Z22, the lower and upper limits of δ_{nd} are set to 0.02 and 0.07 and δ_d to 0.20 and 0.30, respectively. The final $f_d(z)$ is set to the mean value of the upper bounds ($\delta_d = 0.3$ and $\delta_{nd} = 0.07$) and lower bounds ($\delta_d = 0.2$ and $\delta_{nd} = 0.02$). Due to the observed particulate DPR uncertainty, the value of $f_d(z)$ can exceed 1 or below 0, which are set to be 1 and 0, respectively. Finally, we obtain the backscatter profile of dust aerosol as

$$\beta_d(z) = f_d(z) \cdot \beta(z) \quad (\text{B2})$$

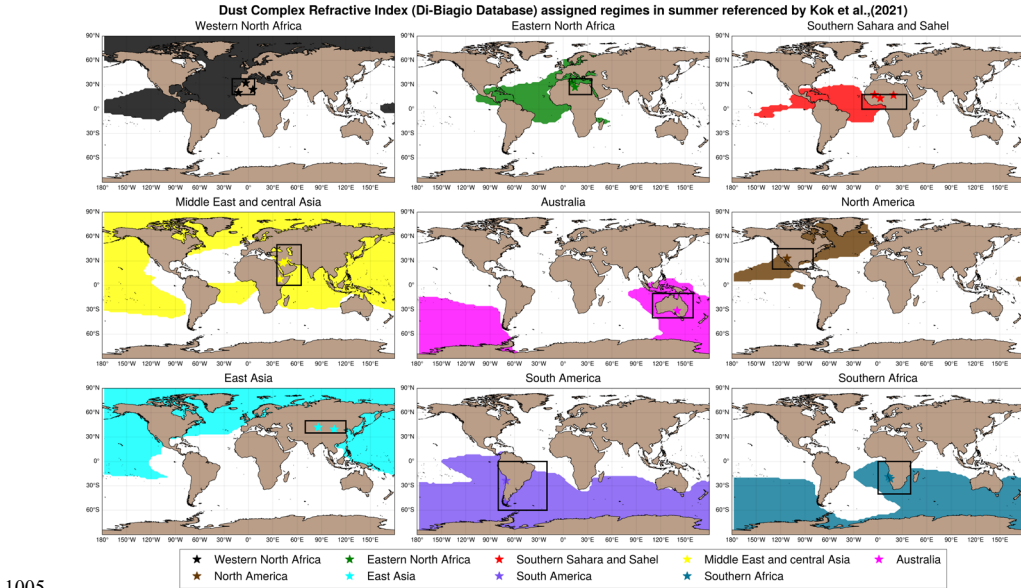
which serves as the dust vertical distribution to scale the input DAOD in the CRTM-DISORT simulation. Note that the extinction coefficient profile can be obtained by multiplying $\beta_d(z)$ with an *a priori* dust extinction-to-backscatter ratios (i.e., Lidar ratios (LR)) for dust aerosol. According to previous studies for the dust LR (Haarig et al., 2022; Liu et al., 2002; Liu et al., 2008; Kim et al., 2020), we further calculate the column integrated DAOD at 532 nm (referred to as “DAOD_{532nm}”) by assuming a dust LR at 44 sr with ± 10 sr uncertainty. However, the DAOD_{532nm} uncertainty contributed by LR is beyond this study and will not be discussed. Readers are referred to Kim et al. (2020) for details.

However, the DPR-based method is likely to include the contribution of sea salt over open oceans and generate non-zero DAOD_{532nm} even without dust, especially in daytime when CALIOP has lower quality due to the solar

990 contamination. The possible reason is that sea salt would have DPR close to dust when their relative humidity is low (e.g., < 50%) (Haarig et al., 2017). Therefore, after deriving DAOD_{532nm}, we further use the CALIOP VFM (i.e., the “Atmospheric_Volume_Description” in the “LID_L2_05kmAPro-Standard-V4” product; see Section 2.1 and Table 1) to filter the profiles that has no dust, or polluted dust or marine dust layers. Finally, the rest of profiles are considered as cloud-free dust profiles for retrievals.

995 **Appendix C: Assignments of dust long-wave refractive index**

Note that assigning dust RIs from different source regions to the observed dust aerosol over the ocean should follow the dust global transport patterns. Accordingly, we applied the fractional contribution over oceans supplied by various dust source regions from the DustCOMM-2021 dataset developed by Kok et al. (2021a). This dataset provides the seasonally resolved global distribution of the fractional contribution of DAOD from nine defined dust source regions (see Figure C1) by integrating observational constraints on dust properties and abundance into an ensemble of GCM simulations, gridded with a resolution of 2.5° longitude by 1.9° latitude. In other words, for each grid cell in each season, there are nine fractions representing the contributions from nine source regions, indicating the probability of where the DAOD that occurs in a grid cell in a particular season originated. We use this data set to choose the appropriate *a priori* dust RIs from different source regions for our retrieval over oceans.



1005 **Figure C1: The assignment of the source region-resolved dust refractive indices from Di Biagio et al. (2017) is based on which of the nine main source regions provided a fractional contribution to SW DAOD that exceeds 0.1, which is shown here for summer based on the DustCOMM-2021 dataset.**

1010 It should be noted that the DustCOMM-2021 is a climatological dataset. As such the uncertainties included in this
dataset cannot be propagated into not propagable for instantaneous observational retrievals. Hence, in this study,
instead of scaling the Di-Biagio RI's fractional contribution to form a new dust RI, we select the source region if its
DAOD fractional contribution exceeds 0.1 and assign the corresponding Di-Biagio RIs within the selected source
region for our retrieval. Figure C1 shows the nine regimes over oceans with fractional contribution greater than 0.1
1015 for the nine defined dust source regions in summer (see Figures S2 to S4 for other seasons). The Di-Biagio RIs are
assigned to the nine source regions based on their geolocations. For observations in each season within each regime,
the retrieval will assume the dust originated from the identified dust source regions and choose the corresponding Di-
Biagio RIs. Note that the nine regimes can overlap, meaning that the observation over a particular grid cell covered
by multiple regimes will assume multiple RIs from these regimes. The uncertainty due to the variation of multiple RIs
1020 is evaluated in Section 3.2.

Data availability

The ~~2007 to 2017~~ MODIS-CALIOP DAOD_{10µm} and coarse-mode D_{eff} data (~~Level 2L2~~ and 5° × 2° monthly ~~Level 3L3~~) ~~from July 2006 to August 2018 will be publicly available at <https://doi.org/10.5281/zenodo.7857132> after the acceptance of this manuscript.~~

1025 Author contribution

Conceptualization, J.Z. and Z.Z.; methodology, J.Z., Z.Z. and Y.H.; software, J.Z., Z.Z., Q.S. and C.W.; validation,
J.Z. and Z.Z.; formal analysis, J.Z.; investigation, J.Z., and Z.Z.; data curation, J.Z., Z.Z., J.F.K., C.D.B., C.R.;
writing—original draft preparation, J.Z.; writing—review and editing, J.Z., Z.Z., Y.H., A.G., Q.S., C.W., J.F.K.,
C.D.B., C.R. and Y.D.; visualization, J.Z.; supervision, Z.Z., Y.H. and A.G.; project administration, Z.Z.; funding
1030 acquisition, Z.Z. All authors have read and agreed to the published version of the manuscript.

Declaration of Competing Interest

Zhibo Zhang reports that financial support was provided by NASA ~~and NSF~~.

Acknowledgment

JZ, ZZ and AG are supported by a NASA grant (no. 80NSSC20K0130) from the CALIPSO and CloudSat program
1035 managed by David Considine. HY was supported by the CloudSat/CALIPSO program. CR acknowledges funding
from NERC grant NE/M018288/1. JFK was supported by NSF grants 1856389 and 2151093 and the Army Research
Office (cooperative agreement number W911NF-20-2-0150). C.D.B. was supported by the Centre National des Etudes
Spatiales (CNES) and by the CNRS via the Labex L-IPSL, which is funded by the ANR (grant no. ANR-10-LABX-

0018). The computations in this study were performed at the UMBC High Performance Computing Facility (HPCF).
1040 The facility is supported by the US National Science Foundation through the MRI program (grant nos. CNS-0821258
and CNS-1228778) and the SCREMS program (grant no. DMS-0821311), with substantial support from UMBC. We
acknowledge the AERIS data infrastructure for providing access to the IASI-LMD data in this study and CNRS-LMD
for the development of the retrieval algorithms. We thank the ICARE Data and Services Center for providing access
to the IASI-ULB data in this study at <http://www.icare.univ-lille1.fr/>. We thank NASA for providing the MODIS and
1045 CALIPSO data, which are available at <https://ladsweb.modaps.cosdis.nasa.gov/> and
<https://asdc.larc.nasa.gov/data/CALIPSO/>. We thank the CloudSat Data Processing Center for providing the MODIS-
AUX data at <https://www.cloudsat.cira.colostate.edu/data-products/modis-aux/>. We also thank the AERONET project
at NASA/GSFC for providing the ground-based aerosol data. The laboratory experiments to retrieve the dust refractive
indices in Di Biagio et al. (2017) that feed this work had received funding from the European Union's Horizon 2020
1050 research and innovation program through the EUROCHAMP–2020 Infrastructure Activity under grant agreement no.
730997. They were supported by the French national programme LEFE/INSU (Les Enveloppes Fluides et
l'Environnement/Institut National des Sciences de l'Univers) and by the OSU–EFLUVE (Observatoire des Sciences
de l'Univers–Enveloppes Fluides de la Ville à l'Exobiologie) through dedicated research funding to the RED-DUST
project. The authors acknowledge the CNRS–INSU for supporting the CESAM chamber as national facility as part of
1055 the French ACTRIS Research Infrastructure as well as the AERIS datacenter (<https://en.aeris-data.fr/>) for distributing
and curing the data produced by the CESAM chamber through the hosting of the EUROCHAMP datacenter
(<https://data.eurochamp.org>). The views and conclusions contained in this document are those of the authors and
should not be interpreted as representing the official policies, either expressed or implied, of the Army Research
Laboratory or the US Government.

1060

References

- Adebiji, A. A. and Kok, J. F.: Climate models miss most of the coarse dust in the atmosphere, *Sci Adv*, 6, eaaz9507, 10.1126/sciadv.aaz9507, 2020a.
- 1065 Adebiji, A. A., Kok, J. F., Wang, Y., Ito, A., Ridley, D. A., Nabat, P., and Zhao, C.: Dust Constraints from joint Observational-Modelling-experimental analysis (DustCOMM): comparison with measurements and model simulations, *Atmos. Chem. Phys.*, 20, 829-863, 10.5194/acp-20-829-2020, 2020b.
- Adebiji, A., Kok, J. F., Murray, B. J., Ryder, C. L., Stuut, J.-B. W., Kahn, R. A., Knippertz, P., Formenti, P., Mahowald, N. M., Pérez Garcia-Pando, C., Klose, M., Ansmann, A., Samset, B. H., Ito, A., Balkanski, Y., Di Biagio, C., Romanias, M. N., Huang, Y., and Meng, J.: A review of coarse mineral dust in the Earth system, *Aeolian Res.*, 60, 100849, <https://doi.org/10.1016/j.aeolia.2022.100849>, 2023.
- 1070 Alizadeh-Chooabari, O., Sturman, A., and Zawar-Reza, P.: A global satellite view of the seasonal distribution of mineral dust and its correlation with atmospheric circulation, *Dynamics of Atmospheres and Oceans*, 68, 20-34, <https://doi.org/10.1016/j.dynatmoce.2014.07.002>, 2014.
- 1075 Amiri-Farahani, A., Allen, R. J., Neubauer, D., and Lohmann, U.: Impact of Saharan dust on North Atlantic marine stratocumulus clouds: importance of the semidirect effect, *Atmos Chem Phys*, 17, 6305-6322, 2017.
- Bagnold, R. A.: *Threshold Speed and Grain Size*, in: *The Physics of Blown Sand and Desert Dunes*, Springer Netherlands, Dordrecht, 85-95, 10.1007/978-94-009-5682-7_7, 1974.
- Capelle, V., Chédin, A., Pondrom, M., Crevoisier, C., Armante, R., Crepeau, L., and Scott, N. A.: Infrared dust aerosol optical depth retrieved daily from IASI and comparison with AERONET over the period 2007–2016, *Remote Sens Environ*, 206, 15-32, <https://doi.org/10.1016/j.rse.2017.12.008>, 2018.
- 1080 Capelle, V., Chédin, A., Siméon, M., Tsamalis, C., Pierangelo, C., Pondrom, M., Crevoisier, C., Crepeau, L., and Scott, N. A.: Evaluation of IASI-derived dust aerosol characteristics over the tropical belt, *Atmospheric Chemistry & Physics*, 14, 2014.
- 1085 Carlson, T. N.: The Saharan elevated mixed layer and its aerosol optical depth, *The Open Atmospheric Science Journal*, 10, 2016.
- Chédin, A., Capelle, V., Scott, N. A., and Todd, M. C.: Contribution of IASI to the Observation of Dust Aerosol Emissions (Morning and Nighttime) Over the Sahara Desert, *J Geophys Res Atmospheres*, 125, e2019JD032014, <https://doi.org/10.1029/2019JD032014>, 2020.
- 1090 Chen, Y., Han, Y., and Weng, F.: Comparison of two transmittance algorithms in the community radiative transfer model: Application to AVHRR, *J Geophys Res Atmospheres*, 117, 10.1029/2011jd016656, 2012.
- Chooabari, O. A., Zawar-Reza, P., and Sturman, A.: The global distribution of mineral dust and its impacts on the climate system: A review, *Atmos Res*, 138, 152-165, 10.1016/j.atmosres.2013.11.007, 2014.
- Clarisse, L., Clerbaux, C., Franco, B., Hadji-Lazaro, J., Whitburn, S., Kopp, A. K., Hurtmans, D., and Coheur, P.-F.: A Decadal Data Set of Global Atmospheric Dust Retrieved From IASI Satellite Measurements, *J Geophys Res Atmospheres*, 124, 1618-1647, <https://doi.org/10.1029/2018JD029701>, 2019.
- 1095 [Clarke, A. D., Shinozuka, Y., Kapustin, V. N., Howell, S., Huebert, B., Doherty, S., Anderson, T., Covert, D., Anderson, J., Hua, X., Moore II, K. G., McNaughton, C., Carmichael, G., and Weber, R.: Size distributions and mixtures of dust and black carbon aerosol in Asian outflow: Physiochemistry and optical properties, *J Geophys Res Atmospheres*, 109, <https://doi.org/10.1029/2003JD004378>, 2004.](https://doi.org/10.1029/2003JD004378)
- 1100 Denjean, C., Cassola, F., Mazzino, A., Triquet, S., Chevaillier, S., Grand, N., Bourriane, T., Momboisse, G., Sellegri, K., Schwarzenbock, A., Freney, E., Mallet, M., and Formenti, P.: Size distribution and optical properties of mineral dust aerosols transported in the western Mediterranean, *Atmos. Chem. Phys.*, 16, 1081-1104, 10.5194/acp-16-1081-2016, 2016.
- 1105 DeSouza-Machado, S. G., Strow, L. L., Hannon, S. E., and Motteler, H. E.: Infrared dust spectral signatures from AIRS, *Geophys Res Lett*, 33, 10.1029/2005gl024364, 2006.
- Di Biagio, C., Banks, J. R., and Gaetani, M.: Dust Atmospheric Transport Over Long Distances, in: *Reference Module in Earth Systems and Environmental Sciences*, Elsevier, <https://doi.org/10.1016/B978-0-12-818234-5.00033-X>, 2021.
- 1110 Di Biagio, C., Formenti, P., Balkanski, Y., Caponi, L., Cazaunau, M., Pangui, E., Journet, E., Nowak, S., Caquineau, S., Andreae, M. O., Kandler, K., Saeed, T., Piketh, S., Seibert, D., Williams, E., and Doussin, J.-F.: Global scale variability of the mineral dust long-wave refractive index: a new dataset of in situ measurements for climate modeling and remote sensing, *Atmos Chem Phys*, 17, 1901-1929, 10.5194/acp-17-1901-2017, 2017.
- 1115 Ding, S., Yang, P., Weng, F., Liu, Q., Han, Y., van Delst, P., Li, J., and Baum, B.: Validation of the community radiative transfer model, *J Quantitative Spectrosc Radiat Transf*, 112, 1050-1064, <https://doi.org/10.1016/j.jqsrt.2010.11.009>, 2011.

- Dubovik, O., Holben, B., Lapyonok, T., Sinyuk, A., Mishchenko, M., Yang, P., and Slutsker, I.: Non-spherical aerosol retrieval method employing light scattering by spheroids, *Geophys Res Lett*, 29, 54-51-54-54, 2002.
- 1120 Dubovik, O., Sinyuk, A., Lapyonok, T., Holben, B. N., Mishchenko, M., Yang, P., Eck, T. F., Volten, H., Munoz, O., and Veihelmann, B.: Application of spheroid models to account for aerosol particle nonsphericity in remote sensing of desert dust, *J Geophys Res Atmospheres*, 111, 2006.
- [Dubovik, O., Smirnov, A., Holben, B., King, M., Kaufman, Y., Eck, T., and Slutsker, I.: Accuracy assessments of aerosol optical properties retrieved from Aerosol Robotic Network \(AERONET\) Sun and sky radiance measurements, *J Geophys Res Atmospheres*, 105, 9791-9806, 2000.](#)
- 1125 Garnier, A., Pelon, J., Dubuisson, P., Yang, P., Faivre, M., Chomette, O., Pascal, N., Lucker, P., and Murray, T.: Retrieval of cloud properties using CALIPSO Imaging Infrared Radiometer: Part II: effective diameter and ice water path, *J. Appl. Meteor. Climatol.*, 52, 2582–2599, <https://doi.org/10.1175/JAMC-D-12-0328.1>, 2013.
- Gasteiger, J., Groß, S., Sauer, D., Haarig, M., Ansmann, A., and Weinzierl, B.: Particle settling and vertical mixing in the Saharan Air Layer as seen from an integrated model, lidar, and in situ perspective, *Atmos. Chem. Phys.*, 17, 297-311, 10.5194/acp-17-297-2017, 2017.
- 1130 Gelaro, R., McCarty, W., Suárez, M. J., Todling, R., Molod, A., Takacs, L., Randles, C. A., Darmenov, A., Bosilovich, M. G., Reichle, R., Wargan, K., Coy, L., Cullather, R., Draper, C., Akella, S., Buchard, V., Conaty, A., da Silva, A. M., Gu, W., Kim, G.-K., Koster, R., Lucchesi, R., Merkova, D., Nielsen, J. E., Partyka, G., Pawson, S., Putman, W., Rienecker, M., Schubert, S. D., Sienkiewicz, M., and Zhao, B.: The Modern-Era Retrospective Analysis for Research and Applications, Version 2 (MERRA-2), *J Climate*, 30, 5419-5454, 10.1175/jcli-d-16-0758.1, 2017.
- 1135 [Giles, D. M., Sinyuk, A., Sorokin, M. G., Schafer, J. S., Smirnov, A., Slutsker, I., Eck, T. F., Holben, B. N., Lewis, J. R., Campbell, J. R., Welton, E. J., Korkin, S. V., and Lyapustin, A. I.: Advancements in the Aerosol Robotic Network \(AERONET\) Version 3 database – automated near-real-time quality control algorithm with improved cloud screening for Sun photometer aerosol optical depth \(AOD\) measurements, *Atmos. Meas. Tech.*, 12, 169-209, 10.5194/amt-12-169-2019, 2019.](#)
- 1140 Ginoux, P.: Effects of nonsphericity on mineral dust modeling, *J Geophys Res Atmospheres*, 108, <https://doi.org/10.1029/2002JD002516>, 2003.
- 1145 Ginoux, P., Garbuzov, D., and Hsu, N. C.: Identification of anthropogenic and natural dust sources using Moderate Resolution Imaging Spectroradiometer (MODIS) Deep Blue level 2 data, *Journal of Geophysical Research-Atmospheres*, 115, 10.1029/2009jd012398, 2010.
- Ginoux, P., Prospero, J. M., Gill, T. E., Hsu, N. C., and Zhao, M.: Global-scale attribution of anthropogenic and natural dust sources and their emission rates based on MODIS Deep Blue aerosol products, *Reviews of Geophysics*, 50, <https://doi.org/10.1029/2012RG000388>, 2012.
- 1150 Gkikas, A., Proestakis, E., Amiridis, V., Kazadzis, S., Di Tomaso, E., Tsekeri, A., Marinou, E., Hatzianastassiou, N., and Pérez García-Pando, C.: ModIs Dust AeroSol (MIDAS): a global fine-resolution dust optical depth data set, *Atmos. Meas. Tech.*, 14, 309-334, 10.5194/amt-14-309-2021, 2021.
- Gkikas, A., Proestakis, E., Amiridis, V., Kazadzis, S., Di Tomaso, E., Marinou, E., Hatzianastassiou, N., Kok, J. F., and Garcia-Pando, C. P.: Quantification of the dust optical depth across spatiotemporal scales with the MIDAS global dataset (2003-2017), *Atmos Chem Phys*, 22, 3553-3578, 10.5194/acp-22-3553-2022, 2022.
- 1155 Goudie, A.: Dust storms in space and time, *Progress in Physical Geography*, 7, 502-530, 1983.
- Grogan, D. F. P., Nathan, T. R., and Chen, S.-H.: Effects of Saharan Dust on the Linear Dynamics of African Easterly Waves, *J Atmos Sci*, 73, 891-911, 10.1175/jas-d-15-0143.1, 2016.
- 1160 Gutleben, M. and Groß, S.: Turbulence Analysis in Long-Range-Transported Saharan Dust Layers With Airborne Lidar, *Geophys Res Lett*, 48, e2021GL094418, <https://doi.org/10.1029/2021GL094418>, 2021.
- Haarig, M., Ansmann, A., Engelmann, R., Baars, H., Toledano, C., Torres, B., Althausen, D., Radenz, M., and Wandinger, U.: First triple-wavelength lidar observations of depolarization and extinction-to-backscatter ratios of Saharan dust, *Atmos. Chem. Phys.*, 22, 355-369, 10.5194/acp-22-355-2022, 2022.
- 1165 Haarig, M., Ansmann, A., Gasteiger, J., Kandler, K., Althausen, D., Baars, H., Radenz, M., and Farrell, D. A.: Dry versus wet marine particle optical properties: RH dependence of depolarization ratio, backscatter, and extinction from multiwavelength lidar measurements during SALTRACE, *Atmos. Chem. Phys.*, 17, 14199-14217, 10.5194/acp-17-14199-2017, 2017.
- Han, Y.: JCSDA community radiative transfer model (CRTM): Version 1, 2006.
- 1170 Hansen, J., Sato, M., and Ruedy, R.: Radiative forcing and climate response, *J Geophys Res Atmospheres*, 102, 6831-6864, 1997.
- Hansen, J. E. and Travis, L. D.: Light scattering in planetary atmospheres, *Space Science Reviews*, 16, 527-610, 10.1007/BF00168069, 1974.

- Hao, M. and Mendel, J. M.: Linguistic Weighted Standard Deviation, 2013 Joint IFSA World Congress and NAFIPS Annual Meeting (IFSA/NAFIPS), 24-28 June 2013, 108-113, 10.1109/IFSA-NAFIPS.2013.6608384,
- 1175 Heckert, N. and Filliben, J.: Dataplot Reference Manual, Volume 2: Let Subcommands and Library Functions, Technical Report 148, National Institute of Standards and Technology, 2003.
- Helmert, J., Heinold, B., Tegen, I., Hellmuth, O., and Wendisch, M.: On the direct and semidirect effects of Saharan dust over Europe: A modeling study, *J Geophys Res Atmospheres*, 112, <https://doi.org/10.1029/2006JD007444>, 2007.
- 1180 [Holben, B. N., Eck, T. F., Slutsker, I., Tanré, D., Buis, J. P., Setzer, A., Vermote, E., Reagan, J. A., Kaufman, Y. J., Nakajima, T., Lavenu, F., Jankowiak, I., and Smirnov, A.: AERONET—A Federated Instrument Network and Data Archive for Aerosol Characterization, *Remote Sens Environ.* 66, 1-16, \[https://doi.org/10.1016/S0034-4257\\(98\\)00031-5\]\(https://doi.org/10.1016/S0034-4257\(98\)00031-5\), 1998.](#)
- Hsu, N. C., Jeong, M.-J., Bettenhausen, C., Sayer, A. M., Hansell, R., Seftor, C. S., Huang, J., and Tsay, S.-C.: Enhanced Deep Blue aerosol retrieval algorithm: The second generation, *J Geophys Res Atmospheres*, 118, 9296-9315, <https://doi.org/10.1002/jgrd.50712>, 2013.
- 1185 Huang, H., Qian, Y., Liu, Y., He, C., Zheng, J., Zhang, Z., and Gkikas, A.: Where does the dust deposited over the Sierra Nevada snow come from?, *EGU sphere*, 2022, 1-38, 10.5194/egusphere-2022-588, 2022.
- Huang, Y., Kok, J. F., Kandler, K., Lindqvist, H., Nousiainen, T., Sakai, T., Adebisi, A., and Jokinen, O.: Climate Models and Remote Sensing Retrievals Neglect Substantial Desert Dust Asphericity, *Geophys Res Lett*, 47, e2019GL086592, <https://doi.org/10.1029/2019GL086592>, 2020.
- 1190 Huneeus, N., Schulz, M., Balkanski, Y., Griesfeller, J., Prospero, J., Kinne, S., Bauer, S., Boucher, O., Chin, M., Dentener, F., Diehl, T., Easter, R., Fillmore, D., Ghan, S., Ginoux, P., Grini, A., Horowitz, L., Koch, D., Krol, M. C., Landing, W., Liu, X., Mahowald, N., Miller, R., Morcrette, J. J., Myhre, G., Penner, J., Perlwitz, J., Stier, P., Takemura, T., and Zender, C. S.: Global dust model intercomparison in AeroCom phase I, *Atmos. Chem. Phys.*, 11, 7781-7816, 10.5194/acp-11-7781-2011, 2011.
- 1195 Journet, E., Balkanski, Y., and Harrison, S. P.: A new data set of soil mineralogy for dust-cycle modeling, *Atmos. Chem. Phys.*, 14, 3801-3816, 10.5194/acp-14-3801-2014, 2014.
- Kahn, R. A., Gaitley, B. J., Garay, M. J., Diner, D. J., Eck, T. F., Smirnov, A., and Holben, B. N.: Multiangle Imaging Spectroradiometer global aerosol product assessment by comparison with the Aerosol Robotic Network, *J Geophys Res Atmospheres*, 115, <https://doi.org/10.1029/2010JD014601>, 2010.
- Kaufman, Y. J., Koren, I., Remer, L. A., Tanre, D., Ginoux, P., and Fan, S.: Dust transport and deposition observed from the Terra-Moderate Resolution Imaging Spectroradiometer (MODIS) spacecraft over the Atlantic ocean, *Journal of Geophysical Research-Atmospheres*, 110, 10.1029/2003jd004436, 2005.
- 1205 Kim, M.-H., Kim, S.-W., and Omar, A. H.: Dust Lidar Ratios Retrieved from the CALIOP Measurements Using the MODIS AOD as a Constraint, *Remote Sens-basel*, 12, 251, 2020.
- Kim, M.-H., Omar, A. H., Tackett, J. L., Vaughan, M. A., Winker, D. M., Trepte, C. R., Hu, Y., Liu, Z., Poole, L. R., and Pitts, M. C.: The CALIPSO version 4 automated aerosol classification and lidar ratio selection algorithm, *Atmos Meas Tech*, 11, 6107, 2018.
- 1210 Kinne, S., Schulz, M., Textor, C., Guibert, S., Balkanski, Y., Bauer, S. E., Berntsen, T., Berglen, T. F., Boucher, O., Chin, M., Collins, W., Dentener, F., Diehl, T., Easter, R., Feichter, J., Fillmore, D., Ghan, S., Ginoux, P., Gong, S., Grini, A., Hendricks, J., Herzog, M., Horowitz, L., Isaksen, I., Iversen, T., Kirkevåg, A., Kloster, S., Koch, D., Kristjansson, J. E., Krol, M., Lauer, A., Lamarque, J. F., Lesins, G., Liu, X., Lohmann, U., Montanaro, V., Myhre, G., Penner, J., Pitari, G., Reddy, S., Seland, O., Stier, P., Takemura, T., and Tie, X.: An AeroCom initial assessment – optical properties in aerosol component modules of global models, *Atmos. Chem. Phys.*, 6, 1815-1834, 10.5194/acp-6-1815-2006, 2006.
- 1215 Kok, J. F., Adebisi, A. A., Albani, S., Balkanski, Y., Checa-Garcia, R., Chin, M., Colarco, P. R., Hamilton, D. S., Huang, Y., Ito, A., Klose, M., Li, L., Mahowald, N. M., Miller, R. L., Obiso, V., Pérez García-Pando, C., Rocha-Lima, A., and Wan, J. S.: Contribution of the world's main dust source regions to the global cycle of desert dust, *Atmos. Chem. Phys.*, 21, 8169-8193, 10.5194/acp-21-8169-2021, 2021a.
- 1220 Kok, J. F., Adebisi, A. A., Albani, S., Balkanski, Y., Checa-Garcia, R., Chin, M., Colarco, P. R., Hamilton, D. S., Huang, Y., Ito, A., Klose, M., Leung, D. M., Li, L., Mahowald, N. M., Miller, R. L., Obiso, V., Pérez García-Pando, C., Rocha-Lima, A., Wan, J. S., and Whicker, C. A.: Improved representation of the global dust cycle using observational constraints on dust properties and abundance, *Atmos. Chem. Phys.*, 21, 8127-8167, 10.5194/acp-21-8127-2021, 2021b.
- 1225 Levy, R., Mattoo, S., Munchak, L., Remer, L., Sayer, A., Patadia, F., and Hsu, N.: The Collection 6 MODIS aerosol products over land and ocean, *Atmos Meas Tech*, 6, 2989-3034, 2013.

- 1230 Li, L., Mahowald, N. M., Miller, R. L., Pérez García-Pando, C., Klose, M., Hamilton, D. S., Gonçalves Ageitos, M., Ginoux, P., Balkanski, Y., Green, R. O., Kalashnikova, O., Kok, J. F., Obiso, V., Paynter, D., and Thompson, D. R.: Quantifying the range of the dust direct radiative effect due to source mineralogy uncertainty, *Atmos. Chem. Phys.*, 21, 3973-4005, 10.5194/acp-21-3973-2021, 2021.
- Li, S.-M., Tang, J., Xue, H., and Toom-Saunty, D.: [Size distribution and estimated optical properties of carbonate, water soluble organic carbon, and sulfate in aerosols at a remote high altitude site in western China](https://doi.org/10.1029/1999GL010929), *Geophys Res Lett.* 27, 1107-1110, <https://doi.org/10.1029/1999GL010929>, 2000.
- 1235 Liang, X., Ignatov, A., Kramar, M., and Yu, F.: Preliminary Inter-Comparison between AHI, VIIRS and MODIS Clear-Sky Ocean Radiances for Accurate SST Retrievals, *Remote Sens-basel*, 8, 203, 2016.
- Liu, C., Panetta, R. L., Yang, P., Macke, A., and Baran, A. J.: Modeling the scattering properties of mineral aerosols using concave fractal polyhedra, *Appl Optics*, 52, 640-652, 2013.
- 1240 Liu, Z., Sugimoto, N., and Murayama, T.: Extinction-to-backscatter ratio of Asian dust observed with high-spectral-resolution lidar and Raman lidar, *Appl Optics*, 41, 2760-2767, 2002.
- Liu, Z., Kar, J., Zeng, S., Tackett, J., Vaughan, M., Avery, M., Pelon, J., Getzewich, B., Lee, K.-P., and Magill, B.: Discriminating between clouds and aerosols in the CALIOP version 4.1 data products, 2019.
- Liu, Z., Omar, A., Vaughan, M., Hair, J., Kittaka, C., Hu, Y., Powell, K., Trepte, C., Winker, D., Hostetler, C., Ferrare, R., and Pierce, R.: CALIPSO lidar observations of the optical properties of Saharan dust: A case study of long-range transport, *J Geophys Res Atmospheres*, 113, <https://doi.org/10.1029/2007JD008878>, 2008.
- 1245 Logothetis, S. A., Salamalikis, V., Gkikas, A., Kazadzis, S., Amiridis, V., and Kazantzidis, A.: 15-year variability of desert dust optical depth on global and regional scales, *Atmos Chem Phys*, 21, 16499-16529, 10.5194/acp-21-16499-2021, 2021.
- Luo, B., Minnett, P. J., Gentemann, C., and Szczodrak, G.: Improving satellite retrieved night-time infrared sea surface temperatures in aerosol contaminated regions, *Remote Sens Environ*, 223, 8-20, <https://doi.org/10.1016/j.rse.2019.01.009>, 2019.
- 1250 Madhavan, S., Xiong, X., Wu, A., Wenny, B. N., Chiang, K., Chen, N., Wang, Z., and Li, Y.: Noise Characterization and Performance of MODIS Thermal Emissive Bands, *Ieee T Geosci Remote*, 54, 3221-3234, 10.1109/TGRS.2015.2514061, 2016.
- 1255 Mahowald, N., Albani, S., Kok, J. F., Engelstaeder, S., Scanza, R., Ward, D. S., and Flanner, M. G.: The size distribution of desert dust aerosols and its impact on the Earth system, *Aeolian Res*, 15, 53-71, 10.1016/j.aeolia.2013.09.002, 2014.
- Marticoarena, B., Chatenet, B., Rajot, J. L., Traoré, S., Coulibaly, M., Diallo, A., Koné, I., Maman, A., Ndiaye, T., and Zakou, A.: Temporal variability of mineral dust concentrations over West Africa: analyses of a pluriannual monitoring from the AMMA Sahelian Dust Transect, *Atmos. Chem. Phys.*, 10, 8899-8915, 10.5194/acp-10-8899-2010, 2010.
- 1260 McConnell, C. L., Highwood, E. J., Coe, H., Formenti, P., Anderson, B., Osborne, S., Nava, S., Desboeufs, K., Chen, G., and Harrison, M. A. J.: Seasonal variations of the physical and optical characteristics of Saharan dust: Results from the Dust Outflow and Deposition to the Ocean (DODO) experiment, *J Geophys Res Atmospheres*, 113, <https://doi.org/10.1029/2007JD009606>, 2008.
- 1265 [McGill, M. J., Vaughan, M. A., Trepte, C. R., Hart, W. D., Hlavka, D. L., Winker, D. M., and Kuehn, R.: Airborne validation of spatial properties measured by the CALIPSO lidar](https://doi.org/10.1029/2007JD008768), *J Geophys Res Atmospheres*, 112, <https://doi.org/10.1029/2007JD008768>, 2007.
- 1270 McMillin, L. M., Xiong, X., Han, Y., Kleespies, T. J., and Van Delst, P.: Atmospheric transmittance of an absorbing gas. 7. Further improvements to the OPTRAN 6 approach, *Appl Optics*, 45, 2028-2034, 10.1364/AO.45.002028, 2006.
- Meng, Z., Yang, P., Kattawar, G. W., Bi, L., Liou, K., and Laszlo, I.: Single-scattering properties of tri-axial ellipsoidal mineral dust aerosols: A database for application to radiative transfer calculations, *Journal of Aerosol Science*, 41, 501-512, 2010.
- 1275 Miller, R. L. and Tegen, I.: Climate Response to Soil Dust Aerosols, *J Climate*, 11, 3247-3267, 10.1175/1520-0442(1998)011<3247:Crtsda>2.0.Co;2, 1998.
- Mishchenko, M. I., Travis, L. D., and Mackowski, D. W.: T-matrix computations of light scattering by nonspherical particles: A review, *J Quantitative Spectrosc Radiat Transf*, 55, 535-575, [https://doi.org/10.1016/0022-4073\(96\)00002-7](https://doi.org/10.1016/0022-4073(96)00002-7), 1996.
- 1280 Mishchenko, M. I., Travis, L. D., Kahn, R. A., and West, R. A.: Modeling phase functions for dustlike tropospheric aerosols using a shape mixture of randomly oriented polydisperse spheroids, *J Geophys Res Atmospheres*, 102, 16831-16847, 1997.

- Müller, D., Lee, K.-H., Gasteiger, J., Tesche, M., Weinzierl, B., Kandler, K., Müller, T., Toledano, C., Otto, S., Althausen, D., and Ansmann, A.: Comparison of optical and microphysical properties of pure Saharan mineral dust observed with AERONET Sun photometer, Raman lidar, and in situ instruments during SAMUM 2006, *J Geophys Res Atmospheres*, 117, <https://doi.org/10.1029/2011JD016825>, 2012.
- Müller, D., Weinzierl, B., Petzold, A., Kandler, K., Ansmann, A., Müller, T., Tesche, M., Freudenthaler, V., Esselborn, M., Heese, B., Althausen, D., Schladitz, A., Otto, S., and Knippertz, P.: Mineral dust observed with AERONET Sun photometer, Raman lidar, and in situ instruments during SAMUM 2006: Shape-independent particle properties, *J Geophys Res Atmospheres*, 115, <https://doi.org/10.1029/2009JD012520>, 2010.
- Nousiainen, T. and Kandler, K.: Light scattering by atmospheric mineral dust particles, in: *Light Scattering Reviews 9: Light Scattering and Radiative Transfer*, edited by: Kokhanovsky, A. A., Springer Berlin Heidelberg, Berlin, Heidelberg, 3-52, 10.1007/978-3-642-37985-7_1, 2015.
- O’Carroll, A. G., Armstrong, E. M., Beggs, H. M., Bouali, M., Casey, K. S., Corlett, G. K., Dash, P., Donlon, C. J., Gentemann, C. L., Hoyer, J. L., Ignatov, A., Kabobah, K., Kachi, M., Kurihara, Y., Karagali, I., Maturi, E., Merchant, C. J., Marullo, S., Minnett, P. J., Pennybacker, M., Ramakrishnan, B., Ramsankaran, R., Santoleri, R., Sunder, S., Picart, S. S., Vázquez-Cuervo, J., and Wimmer, W.: Observational Needs of Sea Surface Temperature, *Frontiers Mar Sci*, 6, 420, 10.3389/fmars.2019.00420, 2019.
- Paepé, B. D. and Dewitte, S.: Dust Aerosol Optical Depth Retrieval over a Desert Surface Using the SEVIRI Window Channels, *J Atmos Ocean Tech*, 26, 704-718, 10.1175/2008jtecha1109.1, 2009.
- Pavolonis, M. J., Heidinger, A. K., and Sieglaff, J.: Automated retrievals of volcanic ash and dust cloud properties from upwelling infrared measurements, *J Geophys Res Atmospheres*, 118, 1436-1458, <https://doi.org/10.1002/jgrd.50173>, 2013.
- Pavolonis, M. J., Sieglaff, J., and Cintineo, J.: Spectrally Enhanced Cloud Objects—A generalized framework for automated detection of volcanic ash and dust clouds using passive satellite measurements: 1. Multispectral analysis, *J Geophys Res Atmospheres*, 120, 7813-7841, <https://doi.org/10.1002/2014JD022968>, 2015.
- Peyridieu, S., Chédin, A., Tanré, D., Capelle, V., Pierangelo, C., Lamquin, N., and Armante, R.: Saharan dust infrared optical depth and altitude retrieved from AIRS: a focus over North Atlantic & comparison to MODIS and CALIPSO, *Atmos Chem Phys*, 10, 1953-1967, 10.5194/acp-10-1953-2010, 2010.
- Peyridieu, S., Chédin, A., Capelle, V., Tsamalis, C., Pierangelo, C., Armante, R., Crevoisier, C., Crépeau, L., Siméon, M., Ducos, F., and Scott, N. A.: Characterisation of dust aerosols in the infrared from IASI and comparison with PARASOL, MODIS, MISR, CALIOP, and AERONET observations, *Atmos. Chem. Phys.*, 13, 6065-6082, 10.5194/acp-13-6065-2013, 2013.
- Pierangelo, C., Mishchenko, M., Balkanski, Y., and Chédin, A.: Retrieving the effective radius of Saharan dust coarse mode from AIRS, *Geophys Res Lett*, 32, 10.1029/2005gl023425, 2005.
- Pierangelo, C., Chédin, A., Heilliette, S., Jacquinet-Husson, N., and Armante, R.: Dust altitude and infrared optical depth from AIRS, *Atmos Chem Phys*, 4, 1813-1822, 10.5194/acp-4-1813-2004, 2004.
- Proestakis, E., Amiridis, V., Marinou, E., Georgoulas, A. K., Solomos, S., Kazadzis, S., Chimot, J., Che, H. Z., Alexandri, G., Biniotoglou, I., Daskalopoulou, V., Kourtidis, K. A., de Leeuw, G., and Ronald, J. V.: Nine-year spatial and temporal evolution of desert dust aerosols over South and East Asia as revealed by CALIOP, *Atmos Chem Phys*, 18, 1337-1362, 10.5194/acp-18-1337-2018, 2018.
- Pu, B. and Ginoux, P.: How reliable are CMIP5 models in simulating dust optical depth?, *Atmos. Chem. Phys.*, 18, 12491-12510, 10.5194/acp-18-12491-2018, 2018.
- Quinn, P. K., Coffman, D. J., Bates, T. S., Miller, T. L., Johnson, J. E., Welton, E. J., Neusüss, C., Miller, M., and Sheridan, P. J.: Aerosol optical properties during INDOEX 1999: Means, variability, and controlling factors, *J Geophys Res Atmospheres*, 107, INX2 19-11-INX12 19-25, <https://doi.org/10.1029/2000JD000037>, 2002.
- Ridley, D. A., Heald, C. L., Kok, J. F., and Zhao, C.: An observationally constrained estimate of global dust aerosol optical depth, *Atmos. Chem. Phys.*, 16, 15097-15117, 10.5194/acp-16-15097-2016, 2016.
- Ryder, C. L., Highwood, E. J., Lai, T. M., Sodemann, H., and Marsham, J. H.: Impact of atmospheric transport on the evolution of microphysical and optical properties of Saharan dust, *Geophys Res Lett*, 40, 2433-2438, <https://doi.org/10.1002/grl.50482>, 2013a.
- Ryder, C. L., Highwood, E. J., Walser, A., Seibert, P., Philipp, A., and Weinzierl, B.: Coarse and giant particles are ubiquitous in Saharan dust export regions and are radiatively significant over the Sahara, *Atmos. Chem. Phys.*, 19, 15353-15376, 10.5194/acp-19-15353-2019, 2019.
- Ryder, C. L., Highwood, E. J., Rosenberg, P. D., Trembath, J., Brooke, J. K., Bart, M., Dean, A., Crosier, J., Dorsey, J., Brindley, H., Banks, J., Marsham, J. H., McQuaid, J. B., Sodemann, H., and Washington, R.: Optical properties of Saharan dust aerosol and contribution from the coarse mode as measured during the Fenec 2011 aircraft campaign, *Atmos Chem Phys*, 13, 303-325, 10.5194/acp-13-303-2013, 2013b.

- 1340 Ryder, C. L., Marengo, F., Brooke, J. K., Estelles, V., Cotton, R., Formenti, P., McQuaid, J. B., Price, H. C., Liu, D., Ausset, P., Rosenberg, P. D., Taylor, J. W., Choulaton, T., Bower, K., Coe, H., Gallagher, M., Crosier, J., Lloyd, G., Highwood, E. J., and Murray, B. J.: Coarse-mode mineral dust size distributions, composition and optical properties from AER-D aircraft measurements over the tropical eastern Atlantic, *Atmos. Chem. Phys.*, 18, 17225-17257, 10.5194/acp-18-17225-2018, 2018.
- 1345 Saito, M., Yang, P., Ding, J., and Liu, X.: A Comprehensive Database of the Optical Properties of Irregular Aerosol Particles for Radiative Transfer Simulations, *J Atmos Sci*, 78, 2089-2111, 10.1175/jas-d-20-0338.1, 2021.
- Scheuvens, D. and Kandler, K.: On composition, morphology, and size distribution of airborne mineral dust, *Mineral Dust*, 15-49, 2014.
- 1350 Scott, N. A. and Chedin, A.: A Fast Line-by-Line Method for Atmospheric Absorption Computations: The Automatized Atmospheric Absorption Atlas, *J Appl Meteorol*, 20, 802-812, 10.1175/1520-0450(1981)020<0802:afblm>2.0.co;2, 1981.
- Shao, Y., Wyrwoll, K.-H., Chappell, A., Huang, J., Lin, Z., McTainsh, G. H., Mikami, M., Tanaka, T. Y., Wang, X., and Yoon, S.: Dust cycle: An emerging core theme in Earth system science, *Aeolian Res*, 2, 181-204, 2011.
- Sokolik, I. N. and Toon, O. B.: Incorporation of mineralogical composition into models of the radiative properties of mineral aerosol from UV to IR wavelengths, *J Geophys Res Atmospheres*, 104, 9423-9444, 1999.
- 1355 Song, Q., Zhang, Z., Yu, H., Kato, S., Yang, P., Colarco, P., Remer, L. A., and Ryder, C. L.: Net radiative effects of dust in the tropical North Atlantic based on integrated satellite observations and in situ measurements, *Atmos Chem Phys*, 18, 11303-11322, 10.5194/acp-18-11303-2018, 2018.
- Song, Q., Zhang, Z., Yu, H., Kok, J. F., Di Biagio, C., Albani, S., Zheng, J., and Ding, J.: Size-resolved dust direct radiative effect efficiency derived from satellite observations, *Atmos. Chem. Phys.*, 22, 13115-13135, 10.5194/acp-22-13115-2022, 2022.
- 1360 Song, Q. Q., Zhang, Z. B., Yu, H. B., Ginoux, P., and Shen, J.: Global dust optical depth climatology derived from CALIOP and MODIS aerosol retrievals on decadal timescales: regional and interannual variability, *Atmos Chem Phys*, 21, 13369-13395, 10.5194/acp-21-13369-2021, 2021.
- 1365 Stamnes, K., Tsay, S. C., Wiscombe, W., and Jayaweera, K.: Numerically stable algorithm for discrete-ordinate-method radiative transfer in multiple scattering and emitting layered media, *Appl Optics*, 27, 2502-2509, 10.1364/ao.27.002502 PMID - 20531783, 1988.
- Stein, A., Draxler, R. R., Rolph, G. D., Stunder, B. J., Cohen, M., and Ngan, F.: NOAA's HYSPLIT atmospheric transport and dispersion modeling system, *B Am Meteorol Soc*, 96, 2059-2077, 2015.
- 1370 Tegen, I. and Fung, I.: Modeling of mineral dust in the atmosphere: Sources, transport, and optical thickness, *J Geophys Res Atmospheres*, 99, 22897-22914, 10.1029/94jd01928, 1994.
- Toledano, C., Torres, B., Velasco-Merino, C., Althausen, D., Groß, S., Wiegner, M., Weinzierl, B., Gasteiger, J., Ansmann, A., González, R., Mateos, D., Farrell, D., Müller, T., Haarig, M., and Cachorro, V. E.: Sun photometer retrievals of Saharan dust properties over Barbados during SALTRACE, *Atmos. Chem. Phys.*, 19, 14571-14583, 10.5194/acp-19-14571-2019, 2019.
- 1375 Uno, I., Eguchi, K., Yumimoto, K., Takemura, T., Shimizu, A., Uematsu, M., Liu, Z., Wang, Z., Hara, Y., and Sugimoto, N.: Asian dust transported one full circuit around the globe, *Nature Geoscience*, 2, 557-560, 10.1038/ngco583, 2009.
- van der Does, M., Knippertz, P., Zschenderlein, P., Giles Harrison, R., and Stuut, J.-B. W.: The mysterious long-range transport of giant mineral dust particles, *Sci Adv*, 4, eaau2768, doi:10.1126/sciadv.aau2768, 2018.
- 1380 Wang, C., Platnick, S., Zhang, Z., Meyer, K., and Yang, P.: Retrieval of ice cloud properties using an optimal estimation algorithm and MODIS infrared observations: 1. Forward model, error analysis, and information content, *J Geophys Res Atmospheres*, 121, 5809-5826, 2016.
- Weinzierl, B., Ansmann, A., Prospero, J. M., Althausen, D., Benker, N., Chouza, F., Dollner, M., Farrell, D., Fomba, W. K., Freudenthaler, V., Gasteiger, J., Groß, S., Haarig, M., Heinold, B., Kandler, K., Kristensen, T. B., Mayol-Bracero, O. L., Müller, T., Reitebuch, O., Sauer, D., Schäfler, A., Schepanski, K., Spanu, A., Tegen, I., Toledano, C., and Walsler, A.: The Saharan Aerosol Long-Range Transport and Aerosol-Cloud-Interaction Experiment: Overview and Selected Highlights, *B Am Meteorol Soc*, 98, 1427-1451, 10.1175/bams-d-15-00142.1, 2017.
- 1390 Wentz, F. and Meissner, T.: AMSR ocean algorithm theoretical basis document, version 2, report, Remote Sens, Syst., Santa Rosa, Calif, 2000.
- [Winker, D. M., Pelon, J., Coakley, J. A., Ackerman, S. A., Charlson, R. J., Colarco, P. R., Flamant, P., Fu, Q., Hoff, R. M., Kittaka, C., Kubar, T. L., Le Treut, H., McCormick, M. P., Mégie, G., Poole, L., Powell, K., Trepte, C., Vaughan, M. A., and Wielicki, B. A.: The CALIPSO Mission: A Global 3D View of Aerosols and Clouds, *B Am Meteorol Soc*, 91, 1211-1230, <https://doi.org/10.1175/2010BAMS3009.1>, 2010.](#)

- 1395 Winker, D. M., Tackett, J. L., Getzewich, B. J., Liu, Z., Vaughan, M. A., and Rogers, R. R.: The global 3-D distribution of tropospheric aerosols as characterized by CALIOP, *Atmos. Chem. Phys.*, 13, 3345-3361, 10.5194/acp-13-3345-2013, 2013.
- Winker, D. M., Vaughan, M. A., Omar, A., Hu, Y., Powell, K. A., Liu, Z., Hunt, W. H., and Young, S. A.: Overview of the CALIPSO Mission and CALIOP Data Processing Algorithms, *J Atmos Ocean Tech*, 26, 2310-2323, 10.1175/2009jtecha1281.1, 2009.
- 1400 Woodage, M. J. and Woodward, S.: U.K. HiGEM: Impacts of Desert Dust Radiative Forcing in a High-Resolution Atmospheric GCM, *J Climate*, 27, 5907-5928, 10.1175/jcli-d-13-00556.1, 2014.
- Woodward, S.: Modeling the atmospheric life cycle and radiative impact of mineral dust in the Hadley Centre climate model, *J Geophys Res Atmospheres*, 106, 18155-18166, <https://doi.org/10.1029/2000JD900795>, 2001.
- 1405 Xia, W., Wang, Y., and Wang, B.: Decreasing Dust Over the Middle East Partly Caused by Irrigation Expansion, *Earth's Future*, 10, e2021EF002252, <https://doi.org/10.1029/2021EF002252>, 2022.
- Xiong, X., Wenny, B. N., Wu, A., Barnes, W. L., and Salomonson, V. V.: Aqua MODIS Thermal Emissive Band On-Orbit Calibration, Characterization, and Performance, *Ieee T Geosci Remote*, 47, 803-814, 10.1109/TGRS.2008.2005109, 2009.
- 1410 Yang, Z., Wang, J., Ichoku, C., Hyer, E., and Zeng, J.: Mesoscale modeling and satellite observation of transport and mixing of smoke and dust particles over northern sub-Saharan African region, *J Geophys Res Atmospheres*, 118, 12, 139-112, 157, <https://doi.org/10.1002/2013JD020644>, 2013.
- Yu, H., Remer, L. A., Kahn, R. A., Chin, M., and Zhang, Y.: Satellite perspective of aerosol intercontinental transport: From qualitative tracking to quantitative characterization, *Atmos Res*, 124, 73-100, <https://doi.org/10.1016/j.atmosres.2012.12.013>, 2013.
- 1415 Yu, H., Chin, M., Remer, L. A., Kleidman, R. G., Bellouin, N., Bian, H., and Diehl, T.: Variability of marine aerosol fine-mode fraction and estimates of anthropogenic aerosol component over cloud-free oceans from the Moderate Resolution Imaging Spectroradiometer (MODIS), *J Geophys Res Atmospheres*, 114, <https://doi.org/10.1029/2008JD010648>, 2009.
- 1420 Yu, H., Chin, M., Winker, D. M., Omar, A. H., Liu, Z., Kittaka, C., and Diehl, T.: Global view of aerosol vertical distributions from CALIPSO lidar measurements and GOCART simulations: Regional and seasonal variations, *J Geophys Res Atmospheres*, 115, <https://doi.org/10.1029/2009JD013364>, 2010.
- Yu, H., Chin, M., Bian, H., Yuan, T., Prospero, J. M., Omar, A. H., Remer, L. A., Winker, D. M., Yang, Y., and Zhang, Y.: Quantification of trans-Atlantic dust transport from seven-year (2007–2013) record of CALIPSO lidar measurements, *Remote Sens Environ*, 159, 232-249, 2015a.
- 1425 Yu, H., Chin, M., Bian, H., Yuan, T., Prospero, J. M., Omar, A. H., Remer, L. A., Winker, D. M., Yang, Y., Zhang, Y., and Zhang, Z.: Quantification of trans-Atlantic dust transport from seven-year (2007–2013) record of CALIPSO lidar measurements, *Remote Sens Environ*, 159, 232-249, 10.1016/j.rse.2014.12.010, 2015b.
- Yu, H., Tan, Q., Chin, M., Remer, L. A., Kahn, R. A., Bian, H., Kim, D., Zhang, Z., Yuan, T., Omar, A. H., Winker, D. M., Levy, R. C., Kalashnikova, O., Crepeau, L., Capelle, V., and Chédin, A.: Estimates of African Dust Deposition Along the Trans-Atlantic Transit Using the Decadelong Record of Aerosol Measurements from CALIOP, MODIS, MISR, and IASI, *J Geophys Res Atmospheres*, 124, 7975-7996, <https://doi.org/10.1029/2019JD030574>, 2019.
- 1430 Yu, Y., Kalashnikova, O. V., Garay, M. J., Lee, H., Choi, M., Okin, G. S., Yorks, J. E., Campbell, J. R., and Marquis, J.: A global analysis of diurnal variability in dust and dust mixture using CATS observations, *Atmos. Chem. Phys.*, 21, 1427-1447, 10.5194/acp-21-1427-2021, 2021.
- 1435 Zhang, H., McFarquhar, G. M., Saleeby, S. M., and Cotton, W. R.: Impacts of Saharan dust as CCN on the evolution of an idealized tropical cyclone, *Geophys Res Lett*, 34, 2007.
- 1440 Zhang, P., Lu, N.-m., Hu, X.-q., and Dong, C.-h.: Identification and physical retrieval of dust storm using three MODIS thermal IR channels, *Global Planet Change*, 52, 197-206, 10.1016/j.gloplacha.2006.02.014, 2006.
- Zheng, J., Huang, X., Sangondimath, S., Wang, J., and Zhang, Z.: Efficient and Flexible Aggregation and Distribution of MODIS Atmospheric Products Based on Climate Analytics as a Service Framework, *Remote Sens-basel*, 13, 3541, 2021.
- 1445 Zheng, J., Zhang, Z., Garnier, A., Yu, H., Song, Q., Wang, C., Dubuisson, P., and Di Biagio, C.: The thermal infrared optical depth of mineral dust retrieved from integrated CALIOP and IIR observations, *Remote Sens Environ*, 270, 112841, <https://doi.org/10.1016/j.rse.2021.112841>, 2022.
- Zhou, Y., Levy, R. C., Remer, L. A., Mattoo, S., Shi, Y., and Wang, C.: Dust Aerosol Retrieval Over the Oceans With the MODIS/VIIRS Dark-Target Algorithm: 1. Dust Detection, *Earth and Space Science*, 7, e2020EA001221, <https://doi.org/10.1029/2020EA001221>, 2020.

1450 Zhou, Y., Levy, R. C., Remer, L. A., Mattoo, S., and Espinosa, W. R.: Dust Aerosol Retrieval Over the Oceans With the MODIS/VIIIRS Dark Target Algorithm: 2. Nonspherical Dust Model, *Earth and Space Science*, 7, e2020EA001222, <https://doi.org/10.1029/2020EA001222>, 2020.